LA-UR-23-22306

Approved for public release; distribution is unlimited.

Title:	Combined Heat Shield and Solar Thermal Propulsion System for an Oberth Maneuver
Author(s):	Benkoski, Jason Joseph Mastandrea, James P. Estacio, Benjamin T. John, Jeremy W. Graffeo, Anna J.
Intended for:	Report
Issued:	2023-03-06

Phase I Final Report
NASA Institute for Advanced Concepts
Combined Heat Shield and Solar Thermal Propulsion System for an Oberth Maneuver

A. INSTITUTIONS:

Los Alamos National Laboratory
Los Alamos, NM 87545

The Johns Hopkins University Applied Physics Laboratory
11100 Johns Hopkins Road, Laurel, MD 20723-6099

B. TITLE OF INVESTIGATION:

Combined Heat Shield and Solar Thermal Propulsion System for an Oberth Maneuver

C. PRINCIPAL INVESTIGATOR:

Dr. Jason J. Benkoski
505-665-3746
jason.benkoski@lanl.gov

D. BUSINESS POINT OF CONTACT:

Ashley Middleton
505-412-2191
middleton@lanl.gov

E. REPORTING MONTH:

Final Report

F. IDENTIFICATION:

NASA NIAC Phase I Study: 21-NIAC22B-0053

G. DATE OF SUBMISSION:

22 February 2023

1. Project Summary

As humanity continues its exploration of space, many space missions are enabled by increases in speed. Examples include outer planet and dwarf planet exploration missions and missions that travel through our solar system into interstellar space. For many of these applications speeds of >10 astronomical units per year (AU/yr) are desired. A powered gravity assist around the Sun may offer the best option for reaching this goal; however, **current** heat shields and kick stages are too heavy or generate too little thrust. Solar thermal propulsion overcomes this tradeoff by converting the heat of the Sun into thrust. By tripling the specific impulse relative to chemical propulsion and by enabling a smaller perihelion through active cooling, this approach nearly doubles the escape velocity.

Our team has designed and built working solar thermal propulsion prototypes out of materials that can survive 2700 K at a 30 x 30 cm scale. These benchtop-scale demonstrations have thus far validated the simplifying assumptions that underlie our thermal and propulsion models. Despite growing confidence that a full-scale heat shield/heat exchanger can survive an Oberth maneuver, many questions remain regarding the feasibility of long-term cryogenic storage of hydrogen propellant.

We therefore performed a full trade study of alternate propellants to determine the maximum escape velocity for a given total system mass, including spacecraft, heat shield, propellant storage, and attitude control system. The main propellants of interest include H_2, LiH, Li, CH_4, and NH_3. The key question is whether alternatives to H_2 enable higher escape velocities by offsetting the loss of specific impulse through reductions in dry mass and system complexity. Our calculations showed, in fact, that lithium, lithium hydrie, and ammonia enable a greater escape velocity than hydrogen when the full system trade is performed. Lithium hydride had the highest escape velocity, at over 12 AU/yr. However, ammonia is more attractive because it removes most of the risk associated with propellant storage and handling. It would allow future TRL advancement to focus on the development of a heat shield that doubles as a heat exchanger for a solar thermal propulsion system. Escape velocities using ammonia are still predicted to exceed 10 AU/yr even if the novel heat shield is unaccompanied by any other technological advances.

2. Mission Context

2.1. Enabled Missions: Dwarf Planets and Interstellar Space

Approximately 130 known dwarf planets (bodies > 400 km diameter inferred to be roughly spherical) inhabit the trans-Neptunian region.[1] Dwarf planets are the most common type of planet in the solar system, far outnumbering the gas giants and terrestrial planets. They are also the least explored. Ceres, Pluto, Charon, and Triton (the latter two often considered as both satellites and dwarf planets) remain the only explored dwarf planets. Also relatively unexplored is the local interstellar medium. Although the Voyager 1 and 2 probes have exited the heliosheath, neither were designed for heliophysics observations. The Pioneer 10 and 11 probes, while in interstellar space, have long ceased functioning; New Horizons, while on an escape trajectory from the Solar System, is not expected to have enough electrical power to remain functional when it finally exits the heliosphere.

To reduce transit times of deep space interstellar exploration missions, high solar system

escape velocities are desired (> 10 AU/yr), as the potentially long transit times pose extreme challenges for both hardware reliability and staffing. The development of high thrust, high specific impulse propulsion systems can thus realize significant cost savings and risk reduction. Consider a mission to the near interstellar medium (~550 AU). Voyager 1–the current record-holder at 3.6 AU/yr–will not journey this far for another 100 years (Fig. 1A). If an interstellar probe were launched today with the same escape velocity as Voyager 1, then all electronics and mechanical systems would have to be designed for a 150-year operational lifetime. Several generations of staff scientists would be required to sustain such a mission.

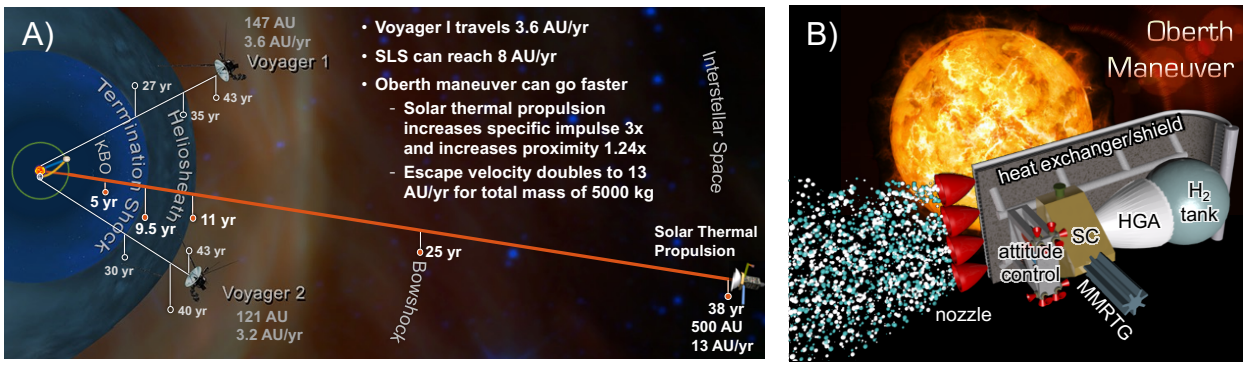

Figure 1. *A) Faster speeds facilitate exploration of KBOs and local interstellar medium. B) A solar thermal propulsion system includes a heat exchanger, propellant tank, and nozzle.*

However, Voyager 1 did not have a trajectory that was optimized for interstellar exploration. We might consider, then, improvements in speed that might be obtained for a purpose-built interstellar probe using advancements that have occurred over the last four decades. An SLS rocket with a Jupiter gravity assist offers improvement, but it tops out at 7-8 AU/yr for a ~1 tonne spacecraft payload.[2] Such speeds still result in a mission duration that approaches 80 years. Perhaps more importantly, the fly-out direction depends on Jupiter's orbital position, and those higher speeds require the fly-out direction to remain close to the ecliptic plane, which can limit science objectives.

The most promising alternative is to perform a powered gravity assist close to the Sun. Also known as an Oberth maneuver, it occurs when a spacecraft falls into the Sun's gravitational well and performs an impulsive burn as it reaches its maximum speed.[3] The asymptotic escape velocity from the solar system (V_{escape}) is given by $V_{escape} = 7.4\ \Delta V^{1/2}\, r_p^{-1/4}$, where ΔV is the change in velocity from the burn, and r_p is the distance from the center of the Sun normalized by the Sun's radius (R_s). Current heat shields and propulsion technology struggle to outperform an unpowered Jupiter gravity assist, let alone 10 AU/yr, due to unfavorable mass tradeoffs.

2.2. New Approach: Combined Heat Shield/Solar Thermal Propulsion

We therefore consider an unconventional approach that tackles both tradeoffs simultaneously–convert the heat of the Sun into usable thrust by passing a fluid through the heat shield (Figure 1B). The elegance of solar thermal propulsion is that it simultaneously increases ΔV and decreases r_p. The specific impulse is three times greater than typical chemical propulsion systems, and the flow of the propellant through the heat shield cools it by several hundred degrees, allowing a closer approach to the Sun. Together, the two effects double the escape velocity

relative to chemical propulsion with a passive heat shield at the same propellant fraction.[5]

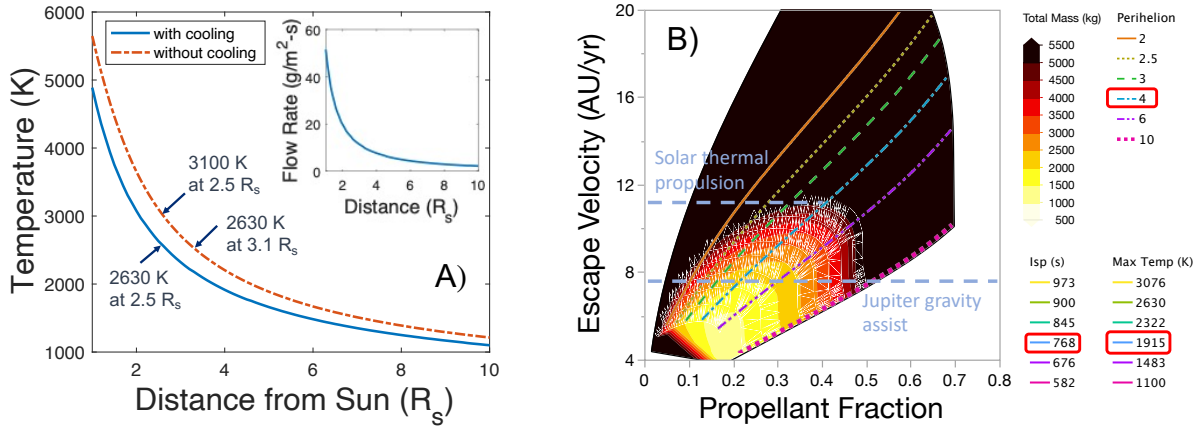

Figure 2. *A) The equilibrium temperature of a heat shield is calculated as a function of distance using the optical properties of our yttria-stabilized zirconia coating and optimized mass flow rate. B) A system mass trade suggests that the maximum achievable escape velocity would be 10.7 AU/yr for a total payload–shield, propulsion system, and spacecraft–of 5000 kg.*

Figure 1B shows a notional design; it consists of a fuel tank, a heat exchanger with a solar-selective coating, and a nozzle. Previous calculations have shown that I_{sp} at 3000 K chamber temperatures can range from 500 s for ammonia up to 1000 s for hydrogen.[4,5] These compare with 317 s for a typical hydrazine bipropellant system.[6] Also beneficial is the active cooling of the heat shield provided by the flowing propellant. Hydrogen has a massive specific heat of 14 J/g-K. A mass flow rate of 15 g/m^2-s cools the surface by 470 K at a perihelion of 2.5 R_s (Figure 2B). Alternatively, it can reduce the perihelion from 3.1 to 2.5 R_s while maintaining constant temperature.

A full system-level mass trade showed that an escape velocity of 10.7 AU/yr could be achieved for a total system mass of 5000 kg, a perihelion of 4 R_s, and shield temperature of 1915 K. The escape velocity was constrained primarily by two factors. The first was the rapid increase in the mass of the heat shield below 4 R_s. The second was the bulkiness of the cryogenic hydrogen storage system. Based on a Lockheed design,[7] the mass ratio of a full 2.3 m diameter H_2 tank is only 2.4-2.8 by itself. The mass ratio drops precipitously once the full mass of the system is included.

To date, solar and nuclear thermal propulsion system designs generally assume that hydrogen is the propellant. With the lowest possible molar mass of 2 g/mol, it provides the greatest thrust on a mass basis. However, the need to store at cryogenic temperature compels additional mass for an insulated tank and cryostat. The question, then, is whether alternative propellants can offset the loss of specific impulse through reductions in dry mass and system complexity.

2.3. Implementation Path

For the past three years, the concept of a combined heat shield and heat exchanger for a solar thermal propulsion system has been demonstrated at the benchtop-scale. These experiments have thus far agreed with theoretical models. In 2020 our team built a benchtop 20 x 20 cm

prototype out of Inconel 718 alloy using an additive manufacturing process. We also built an outdoor solar simulator test station (Figure 3) that can illuminate a 20 x 100 cm area at an intensity equivalent to 20 Suns.

In 2021, we extended our proof-of-concept by building the entire prototype out of materials that can survive a solar Oberth maneuver, which requires them to withstand vacuum at 2500 K for at least four hours. The second prototype design is shown in Figure 4. It consists of a carbon-silicon carbide composite that can survive up to 3003 K, a yttrium oxide coating that can survive up to 2698 K, and a rhenium interlayer that can survive up to 3458 K. By co-developing the high temperature materials together with the solar thermal propulsion system, we can demonstrate the survivability and manufacturability of the proposed system. Comparison of experimentally determined thrust and thermal data with theory has also been used to build confidence in models that suggest significant benefits of this approach, which include the ability to reach an escape velocity > 10 AU/yr.

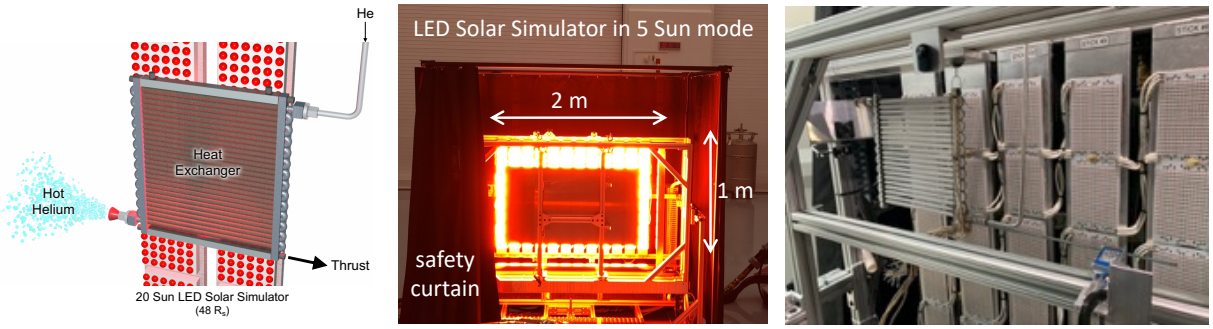

Figure 3. *The outdoor solar simulator test station provided illumination over a 0.2 m^2 area up to 20 Sun equivalent illumination. It could be used to measure the thrust generated by passing helium gas through benchtop prototoypes.*

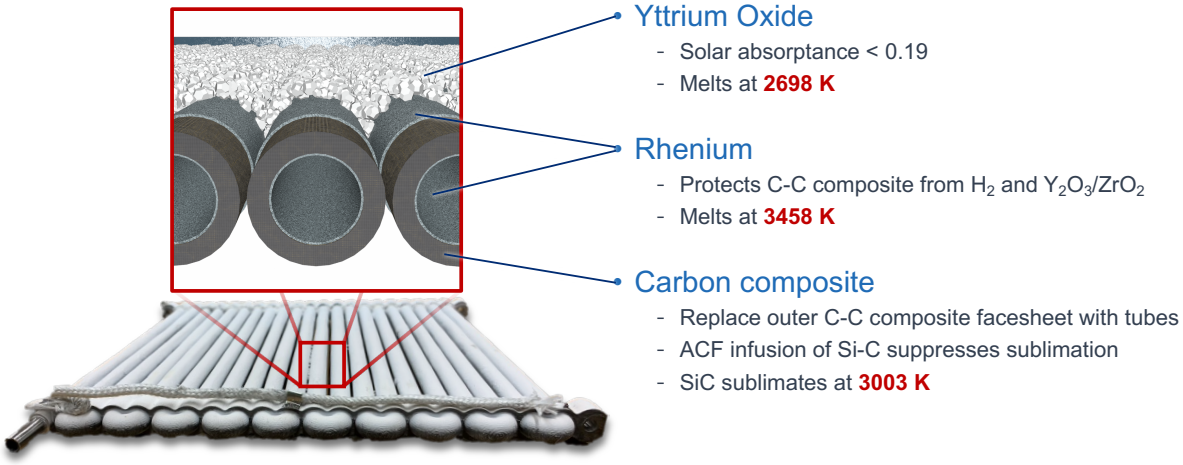

Figure 4. *The 2021 prototype is made entirely from materials that can survive up to 2698 K. Carbon composite forms the primary structure. A conformal rhenium coating protects the graphite from chemical reactions with the hydrogen propellant and the metal oxide coating. A white coating of yttrium oxide reflects sunlight while passively radiating heat in the form of infrared light.*

As the experiments were designed to demonstrate, Figure 5 shows only minor discrepancies between theory and measurement. Figure 5A shows good agreement between the predicted temperature and measured temperature of the white yttrium oxide coating. Figure 5B shows that the predicted level of cooling from the hydrogen gas was consistent with thermocouple readings near the inlet of the prototype, where most of the heat absorption was occurring. Lastly, Figure 5C shows that the measured specific impulse was within 10% of the predicted value. This small deviation can be explained by a small amount of leakage at the joints between the manifolds and tubes.

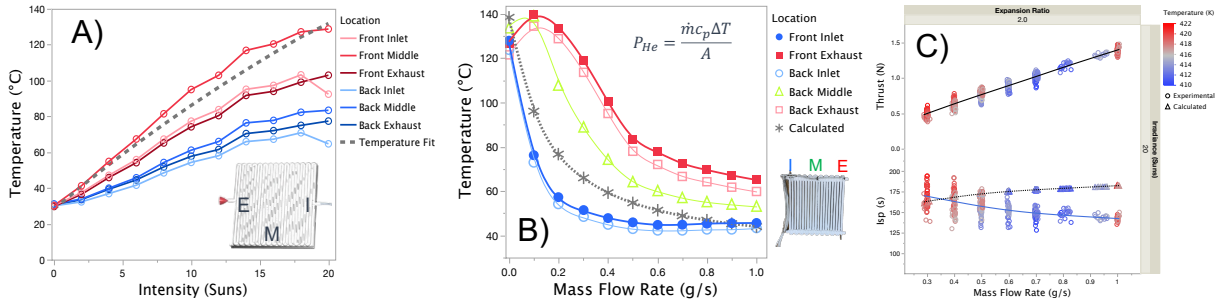

Figure 5. *A) The calculated temperature was consistent with the measured value near the center of the prototype. B) The predicted cooling effect of the flowing helium gas was consistent with measurements and the fact that most of the cooling takes place near the inlet. C) The measured thrust was slightly lower than expected due to the fact that the joints in the prototype had some minor leakage.*

In 2022, JHU/APL and Advanced Ceramic Fibers, LLC (ACF) constructed a 30 x 30 cm prototype using high temperature refractory materials, and tested it at the National Solar Thermal Test Facility (NSTTF). NSTTF has the capacity to operate at 2500 Suns over that spot size, which is equivalent to a perihelion of 4.3 solar radii. The test was also performed with helium propellant in the interest of safety. Although the intense thermal gradient from front to back caused a fissure to run parallel to the surface along the mid-plane, the prototype otherwise survived the extreme heating in air. The test matures this technology to a TRL of 3. Early results show strong promise for the feasibility of manufacturing a solar thermal propulsion heat exchanger at the scale of the Parker Solar Probe (PSP) thermal protection system and at a similar mass.

Our ongoing the technology roadmap has not proceeded along the typical order (Figure 6). It began with breadboard prototypes rather than material coupons. We reasoned that materials could always be found that could individually survive the extreme conditions of a solar Oberth maneuver. However, we were less convinced that it would be possible to manufacture such materials into a complex heat shield geometry, let alone integrate them with other refractory materials. We therefore opted to manufacture prototypes of increasing size: 10 x 10 cm, 20 x 20 cm, and 30 x 30 cm.

Not only would all materials need to survive the operational conditions, but so would their interfaces and geometry. Therefore, the plan was to begin with a relatively mature design, but relatively less mature materials. With each iteration, the materials improved, and the testing shifted towards increasingly realistic conditions. Doing so has allowed our team to rapidly assess the aspects of the technology that required the most maturation, and focus our efforts there.

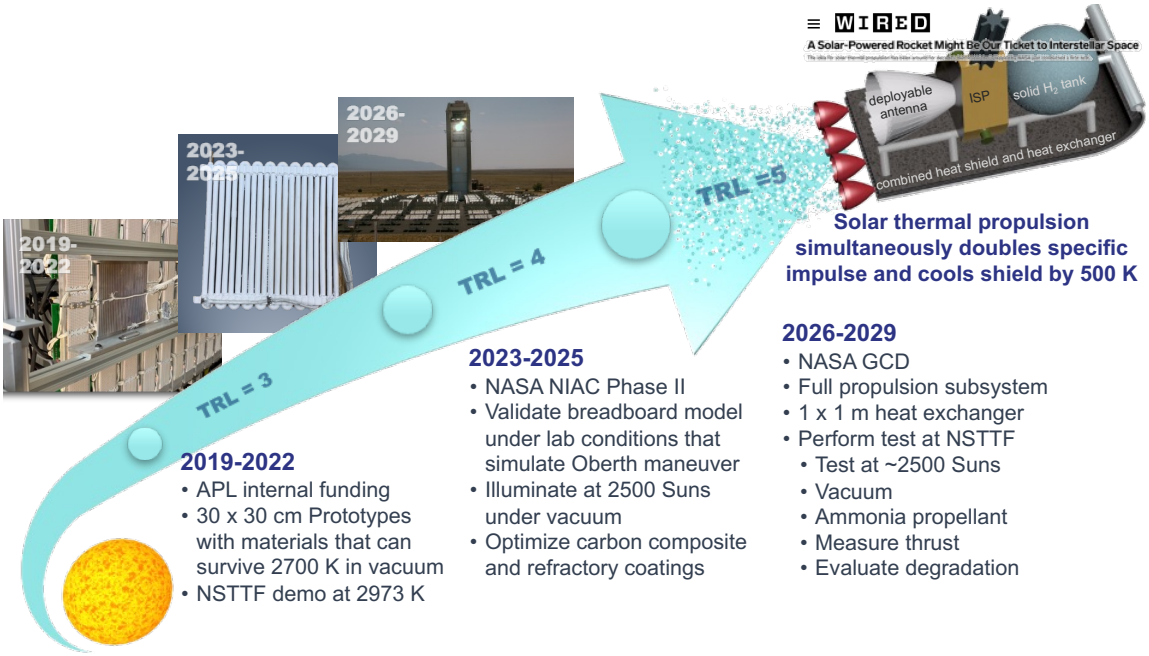

Figure 6. *Technology roadmap from TRL 3 to 5.*

The current study fills an important gap in the above effort, as the propellant storage and handling system may carry a similar level of risk as the combined heat shield and heat exchanger. Depending upon the optimal propellant, the implementation path in a Phase II NIAC would begin with the design and fabrication of a benchtop-scale propellant storage and handling system. The effort will look very different depending on whether liquid ammonia or a solid propellant such as LiH is selected. This development process would be accelerated by the access to the heat exchangers and nozzles being developed for the parallel effort. The goal would be to reach a TRL of 4 by the end of Phase II (FY26), and then develop a plan to reach TRL 5 or 6 at the end of a three-year Game Changing Development (GCD) program (FY29).

Subsequent maturation to TRL 9 depends on the outcome of upcoming NASA decadal surveys. The Interstellar Probe has been discussed in the past two Heliophysics Decadal Surveys[8, 9] and by the general community long before.[10] JHU/APL leads an ongoing study supported by NASA to provide technical input for the deliberations of the 2023-2032 Heliophysics Decadal Survey. An argument can be made that a solar Oberth maneuver with a combined heat shield and solar thermal propulsion systems is one of the few conceivable technologies that can achieve the science objectives of an interstellar mission in its entirety.

2.4. Potential Impact

We have taken a uniquely holistic view of the system to optimize the heat shield and propulsion system together. The large specific heat capacity of the propellant combined with the large endotherms of vaporization and thermolysis make it possible to achieve significant improvements in proximity. To make exploration of interstellar space a practical reality it would be necessary to travel up to 6x faster than any man-made object has traveled before. This will not be possible through incremental improvements in kick stages and heat shields. A completely new approach is required. If solar thermal propulsion indeed makes 20 AU/yr possible, then

deep space missions may become more commonplace. The Oberth Maneuver may also provide a unique opportunity to study the Sun as the gas-cooled heat shield allows deeper penetration into the corona than ever before.

Our solar thermal propulsion concept is inspired by Dragonfly, the recently awarded New Frontiers mission to Titan. Dragonfly combines the exciting science of exploring Titan for signs of life with the engineering feat of flying a nuclear-powered dual quad copter autonomously in Titan's atmosphere. With our NIAC concept, we hope to do the same: combine the exciting science of interstellar space with a spacecraft that shatters previous records for man-made vehicles with respect to operating temperature, speed, distance from the Earth, and longevity. To do so with a solar powered rocket makes the mission that much more engaging.

Additional benefits of heat shield technology advancements would be to enable planetary probe mission concepts that require rapid deceleration in order to be captured by a planetary body. Advancements in heat shields and heat transfer would increase aerobraking capabilities by using the heat of re-entry to provide propulsion in the opposite direction to be gravitationally captured.

Advances in materials and manufacturing that arise from this technology have further implications for our renewed interest in nuclear thermal propulsion. Nuclear thermal propulsion is functionally identical to solar thermal propulsion except that the heat source comes from nuclear fuel. It has many of the same design considerations, particularly with respect to the selection of refractory materials. Thus, most of the technological advances in this study will have direct implications for nuclear thermal propulsion.

Beyond space, this technology also benefits endoatmospheric applications such as hypersonic travel. For the former, consider how active cooling of the aeroshell could extend the maximum velocity of a hypersonic vehicle. The increasing specific impulse with increasing temperature creates a virtuous cycle whereby propulsion becomes more efficient with increasing speed. A combined heat exchanger and aeroshell with appropriate nozzles could maintain or even increase velocity as it overcomes drag.

Perhaps less directly, the suite of technologies that we are developing will be relevant for power production. Nuclear fission reactors and nuclear fusion reactors both benefit from high temperature materials and involve active cooling. Even less obvious aspects such as the ability to withstand pressurization at high temperature and performance in vacuum come into play. Moreover, any development of new materials or processes to address the extreme temperatures, radiation, and vacuum of a solar Oberth maneuver will create new infrastructure that will benefit the aerospace, transportation, and energy sectors.

2.5. Significant Technical Challenges

Having demonstrated solar thermal propulsion prototypes with materials that can survive 2700 K at a benchtop scale, we have growing confidence that a heat shield/heat exchanger can survive an Oberth maneuver. Our attention now turns towards the propellant. Even granting the high specific impulse of H_2, many questions remain regarding the feasibility of long-term cryogenic storage.

Both the Spitzer and Wide-Field Infrared Survey Explorer (WISE) demonstrated long-term storage of cryogens without the need for cryocoolers.[11] Though Spitzer achieved an operational

mission duration of 5 years, the boil-off rate would be unacceptable for an Oberth maneuver. A Lockheed Martin report in 2003 addressed this issue by detailing a tank design that would store solid hydrogen at 27 K for 3.6 years.[7] The large tank necessitates a commensurate heat shield. This unfavorable tradeoff is the primary constraint on the escape velocity. Any boil-off or other deviations from these assumptions negate the advantages relative to a Jupiter gravity assist.

The main question with this approach has been–and remains–where is the inflection point on performance given that the thermal shield mass is going to increase with decreasing perihelion? The size and mass of cryogenic storage compels the exploration of alternatives. An intriguing possibility is lithium hydride. A solid at room temperature, it melts at 962 K, and boils at 1220 K. The 4.84 J/g-K specific heat is lower than hydrogen, but the 27 kJ/g latent heat of vaporization more than compensates.[12] Perhaps most tantalizing is the average molar mass of 3.5 g/mol when fully dissociated. CH_4 and NH_3 will also be considered due to their relaxed storage requirements. Although they have a lower specific impulse than H_2, higher mass ratios are much easier to achieve. A full mass trade may reveal higher escape velocities for hydrogen.

2.6. Alternative Approaches

The high specific impulse of solar thermal propulsion, combined with its ability to generate high thrust, has drawn serious consideration for orbit transfer from LEO to GEO.[13] It has also been proposed for small satellite applications, because it could generate greater thrust with lower consumption of onboard power than competing high efficiency propulsion systems.[14, 15, 16] Developments on this technology date back to the 1950's.[17, 18, 19]

The key innovation for our specific embodiment of solar thermal propulsion is the use of a combined heat exchanger and heat shield during a powered gravity assist around the Sun. It is a rare application where the biggest challenge is not increasing the temperature to maximize efficiency, but rather overheating due to the excessive illuminance (3000 Suns = 4.1 MW/m^2). Most embodiments of solar thermal propulsion consider near-Earth orbit, where overheating is not a concern. The challenge instead is that the illuminance (1 Sun = 1.4 kW/m^2) will heat most dark surfaces to 400-500 K, or perhaps 600 K on a spectrally selective surface.[20, 21]

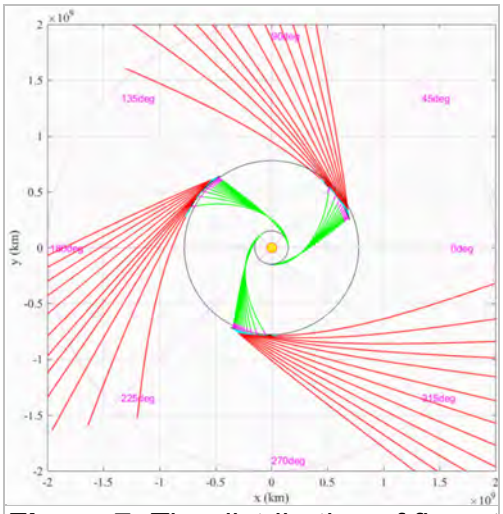

Figure 7. *The distribution of fly-out directions for a passive Jupiter gravity assist as C_3 varies. Figure taken from reference 38.*

Previous discussions of solar thermal propulsion therefore centered on maximizing temperature of the heat exchanger to maximize specific impulse. Rather than reflect sunlight to prevent material degradation under the extreme operating conditions of a solar Oberth maneuver, these designs did the opposite; they included a solar concentrator and absorber to achieve the highest temperature possible for a given size and mass.[22, 23, 24] Melting, boiling, and heat absorption of a propellant were not considered as a means of active cooling to improve the survivability of the heat exchanger.

The idea of using solar thermal propulsion for deep space missions is relatively new.[25, 26, 27]

There are few precedents for such missions, so direct comparisons with alternative approaches are not readily available. Some have proposed the use of a solar sail in a powered gravity assist around the Sun,[28, 29, 30, 31] or acceleration with Earth-based lasers.[32, 33, 34] Others still have proposed nuclear thermal propulsion[35, 36] and ionic propulsion[37]. Arguing the benefits of our approach against these alternatives is premature, because full system designs do not yet exist. Performance estimates are based on a set of assumptions whose accuracy corresponds to the technology readiness level, which varies greatly across this set of examples.

A better comparison might be made with currently available technology. Three years ago, JHU/APL concluded a study of the feasibility of an interstellar probe mission that could be performed by the year 2030. They considered a pragmatic interstellar probe with the ability to operate at 1000 AU and a design lifetime of 50 years. This study was performed for the NASA Heliophysics Division. The team's 2019 report[38] considered three approaches for reaching interstellar space using currently available technologies.

1. Passive Jupiter gravity assist
2. Powered Jupiter flyby
3. Solar Oberth maneuver

It was clear that the required characteristic energy (C_3) for these trajectories could only be realized with a sizable upper stage and between the EUS of the SLS Block 1B and the Star 48BV powered stage.[39] Calculations showed that the powered Jupiter gravity assist (Option 2) did not trade well against a passive Jupiter gravity assist (Option 1) with a much larger launch C_3.

A passive Jupiter gravity assist can achieve 7-8 AU/yr with a launch C_3 between 200 and 300 km^2/s^2. Figure 7 shows the distribution of fly-out directions. Observe how limited they are as the C_3 varies for three different fly-out windows. The small spread is a major disadvantage of the passive Jupiter gravity assist. Additionally, these higher speeds require the fly-out direction to remain close to the ecliptic plane, which can limit science objectives.

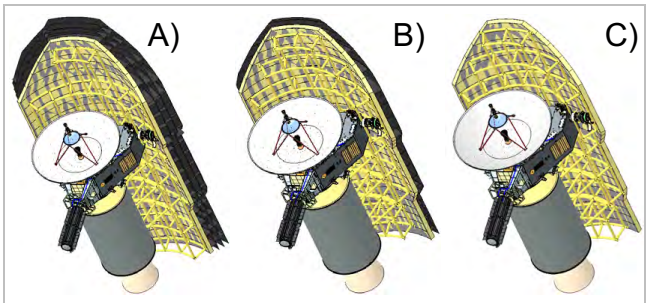

Figure 8. *Orion 50XL stack with thermal shield for perihelia of 3 solar radii (A), 4 solar radii (B), and 5 solar radii (C). Figure taken from reference 38.*

The final option considered was a solar Oberth maneuver. They confined system concepts to existing technologies. Of the kick stages considered, only the Orion 50XL stack, shown in Figure 8, could be launched directly to Jupiter with an SLS rocket. The calculated escape velocity for a solar Oberth maneuver was about 9 AU/yr. Despite the increased speed, it would take 50 years to overtake the passive Jupiter gravity assist because of the 3-year transit time to the Sun. The study's conclusion, then, was that a solar Oberth maneuver would not be worth the risk using **current** rocket stages.

The report concluded by noting that the increased specific impulse of technologies such as solar or nuclear thermal propulsion would have an enormous impact on the mission profile. Simply increasing the specific impulse to I_{sp} of 900 s would double the escape velocity. While noting that solar or nuclear thermal propulsion are the only viable options to achieve that value, both were eliminated from consideration in this trade study due to the inability to cryogenically

store hydrogen for the 2-year transit to the Sun using **current** storage technologies. To date, no alternative propellant has been proposed. Cryogenic storage by itself would not be disqualifying but for the fact that a solar Oberth maneuver requires a 2-year transit. Either boil off must be prevented for the entire duration within a reasonable mass envelope or an alternative propellant must be chosen. Otherwise, the escape velocity from the solar system will be capped at 7-8 AU/yr for the foreseeable future.

3. Phase I Technical Progress

3.1. Technical Approach

The analytical approach for this study is modeled after the approach that JHU/APL previously used to design the thermal protection system for Parker Solar Probe. In order, the mass trade analysis consists of nine calculations.

1. Propellant storage and handling system mass and volume as a function of propellant mass
2. Umbra angle as a function of perihelion
3. View factor of the back of the heat shield to space
4. Required shield thickness as a function of surface temperature
5. Shield mass as a function of propellant mass
6. Total wet mass of the system as a function of propellant mass
7. Surface temperature as a function of perihelion and mass flow rate
8. Specific impulse as a function of surface temperature
9. Escape velocity as a function of wet mass, dry mass, and perihelion.

The first step is the key task in this effort. The underlying design assumptions have been based on reasonable analogs from heritage systems, and from published design concepts in the open literature.

The umbra angle behind the heat shield becomes significant for a perihelion less than 10 solar radii. This calculation determines how much wider the heat shield needs to be than the payload to ensure that all components remain in shadow. For the third step, we calculate the view factor from the back of the heat shield to the bottom of the spacecraft bus by approximating the payload as a cylinder with the same length as the heat shield.

The minimum thickness of the heat shield is governed by the maximum amount of heat that can be absorbed by the spacecraft bus (50 W). The emissivity of the carbon composite then gives the maximum allowable temperature of the back side of the heat shield. Once the temperature gradient across the shield is known, the temperature-dependent thermal conductivity of the carbon foam determines the panel thickness. Having calculated area and thickness, we then apply the average density to derive the heat shield mass. The heat shield properties have taken from experimentally determined values for Parker Solar Probe.

With masses for the spacecraft, antenna, attitude control system, heat shield, and propellant storage system known, the maximum mass ratio (wet mass/dry mass) can be determined for a given rocket payload (5000 kg). If the calculation is performed as a function of perihelion, it will be possible to calculate I_{sp}, and then ΔV. Recalling that $V_{escape} = 7.4\ \Delta V^{1/2}\, r_p^{-1/4}$, one obtains the escape velocity as a function of total system mass. This calculation ultimately determines which propellant gives the greatest escape velocity for a given payload mass envelope when the

cascading effects on the mass of the total system are fully accounted for.

3.1.1. Propellant Storage and Handling System

The first step in evaluating the selection of propellant from a system standpoint is to understand how the mass of the propellant storage and handling system scales with the mass of propellant. Propellants that are stored under pressure require tanks with thick walls and propellants requiring cryogenic storage require insulation and cryostats. Each adds unwanted dry mass to the system which decreases the mass ratio, and therefore ΔV. In our analysis, we consider multiple components in addition to the tank, such as heating stages, fluid pumps, valves, tubing, and sensors. Each are considered on a case-by-case basis.

Also considered in this analysis is material compatibility. In particular, hydrogen causes embrittlement in many alloys, and lithium is a powerful reducing agent. Compounding these issues are various chemical reactions that only take place at elevated temperatures, for which data is scant. Take, for example, the thermal decomposition of methane which leaves carbon deposits on cooler surfaces in the gas flow path.[40] Lithium will ionize above 3500 K to form a plasma.[41] Hydrogen will react with carbon composites to form hydrocarbons.[42] We therefore began our analysis by compiling a list of compatible materials that could be used to store each propellant. Literature reviews yielded key information for hydrogen,[7] lithium,[43] and lithium hydride[44,45]. The full list is provided in Table 1.

***Table 1**. List of compatible tank materials for each propellant*

Propellant	Tank Material	Density (kg/m3)	Young's Modulus (GPa)	Ultimate Tensile Strength (MPa)	Yield Strength (MPa)
Hydrogen	Al 2219	2850	72	434	345
Hydrogen	AlLi 8090	2550	79	462	338
Hydrogen	AlLi UL50	2300	91	379	310
Hydrogen	Graphite-Epoxy Composite	1500	130	1200	N/A
Lithium	Iron	7870	200	540	50
Lithium	Low Carbon Steel (Ti and Nb doped)	7870	205	440	370
Lithium	Ferritic Stainless Steel (441)	7870	220	470	270
Lithium	Austenitic Stainless Steel (316)	8000	193	605	290
Lithium	Molybdenum (Mo0.5-Ti-0.08Zr)	10300	330	324	
Lithium	Tantalum (T-111 alloy)	16650	186	900	705
Lithium	Niobium	8570	103	275-585	70
Lithium	Zirconium	6530	94.5	330	230
Lithium	Titanium	4505	100	240-360	240
Lithium	Tungsten	19300	400	980	750
Lithium	Rhenium	21030	469	1070	290
Lithium	Vanadium	6110	125.5	800	776
Lithium Hydride	CRES 304L	8000	193	485	170

Lithium Hydride	CRES 304	8000	193	515	205
Lithium Hydride	CRES 316L	8000	193	485	170
Lithium Hydride	CRES 309	8000	200	620	310
Lithium Hydride	Armco Iron				
Lithium Hydride	CRES 312	8000	200	780	510
Lithium Hydride	CRES 347	7700-8030	190-210	480	205
Lithium Hydride	Low Carbon Steel (0.06% Ti and 0.07% Nb)	7870	205	440	370
Ammonia	Carbon Steel (1080)	7700-8030	190-210	965	585
Ammonia	CrNi(Mo) steel (34CrNiMo6 Steel)	7780	210	800-1400	600-1000
Ammonia	CRES 304L	8000	193	485	170
Ammonia	Al 7075	2810	71.7	572	430-480
Ammonia	Ti-6Al-4V	4430	114	1170	1100
Methane	AlLi-2198	2700	76.5	462-476	407-427
Methane	CRES 304L	8000	193	485	170
Methane	Al 7075	2810	71.7	572	430-480
Methane	Ti-6Al-4V	4430	114	1170	1100

For this mass trade, the propellant tank mass serves as a proxy for overall propulsion system mass impact. A specific point design for each system was not generated but rather a notional system layout was presented, which captured major functions for the system. The propulsion device performance was not evaluated in the study.

For each propellant option, propellant tank size was considered over a range of propellant mass, from 50 to 250 kg. Tank mass was calculated based on the required volume for each propellant, maximum expected operating pressure (MEOP), and material selection. For the current study, only metal tanks were considered with titanium, aluminum, and stainless steel. In all cases, titanium tanks offered the lowest mass solution while the stainless steel tanks were the highest mass. This analysis indicated that lithium hydride would have the lowest tank mass of all options considered.

Based strictly on the mass of the propellant storage and handling system, ammonia would likely be the best propellant option for a solar thermal propulsion system. While not the lowest mass solution, it is the second lowest mass solution. However, the much lower system complexity of ammonia versus the lithium hydride option would provide the lowest system mass solution. As a storable liquid, there is no need for a complex thermal management system, whether comparing to high temperatures for solid propellant or at low temperatures for cryogenic propellant.

Future work would include a detailed concept design to identify specific components for the propellant choice and evaluate the thruster performance impacts. On thruster performance, the development of requirements for the flow system would be derived to ensure adequate propellant flow to meet performance expectations. This will influence the final selection of the propellant, as this will drive mass flow rates to the thruster.

3.1.1.1. Hydrogen

In 2003 Lockheed-Martin performed a detailed analysis to design a concept for a cryogenic tank that could store solid hydrogen during the two-year transit from Earth to Jupiter, and then from Jupiter to the Sun, following a passive gravity assist.[7] They assumed a spherical tank with a non-vented design that stored hydrogen in solid form (Figure 9). It was rated to 74 psi, and it had a specially designed vacuum shell that could be deployed after it leaves atmosphere. The shell deployment would then reduce the dry mass, which, in turn would increase the ΔV for the given quantity of hydrogen. The hydrogen mass and wet mass of the tank both scale quadratically with radius.

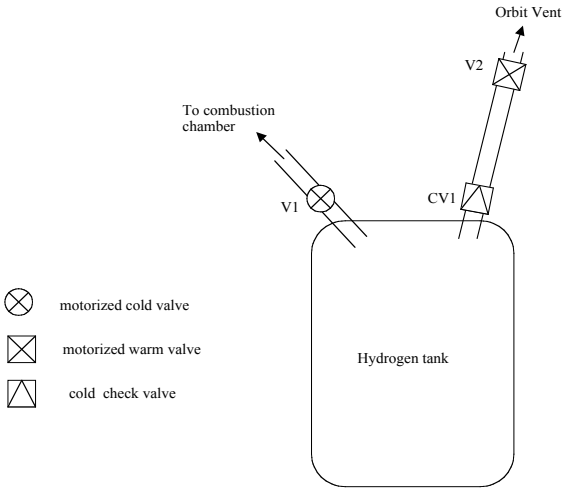

Figure 9. *Lockheed's plumbing schematic and valve operations for a non-vented cryogenic hydrogen tank.*[7]

Four materials were considered in all: 2219 Aluminum, 8090 Aluminum, UL50 Al-Li, and a graphite fiber-epoxy composite. The composite tank had by far the smallest mass penalty. Further maturation of this technology might render it a feasible option for the hydrogen tank, but for this analysis we selected the Al 8090 alloy. Though denser than the composite, it is currently available in sufficient quantities for this application. Additionally, it is more consistent in density and strength to the aluminum alloys that were chosen for the other propellants, which provides a more direct comparison. Observe that the previous mass calculations for hydrogen propellant shown in Figure 2B used the graphite-epoxy composite.

3.1.1.2. Lithium Hydride

The components in a lithium hydride system would include a propellant tank, fluid pump, propellant liquefying heater, pump, and associated valves, tubing, and sensors (Figure 10). These components are assumed to be constant in relation to mass impact. The system mass with these assumptions is therefore driven by tank design and the material selected. In this design, solid propellant is assumed at 100 psi to feed liquid into the flow control system. Based on compatibility with lithium hydride, we considered Ti-6Al-4V, 304 stainless steel, and Al 7075. The scaling of subsystem mass with lithium hydride mass is given below.

Ti-6Al-4V: $m_{sub} = 1.065 m_{LiH} + 2 \times 10^{-7}$

304 Stainless Steel: $m_{sub} = 0.8093 m_{LiH} + 2 \times 10^{-6}$

Al 7075: $m_{sub} = 0.1203 m_{LiH} - 4 \times 10^{-7}$

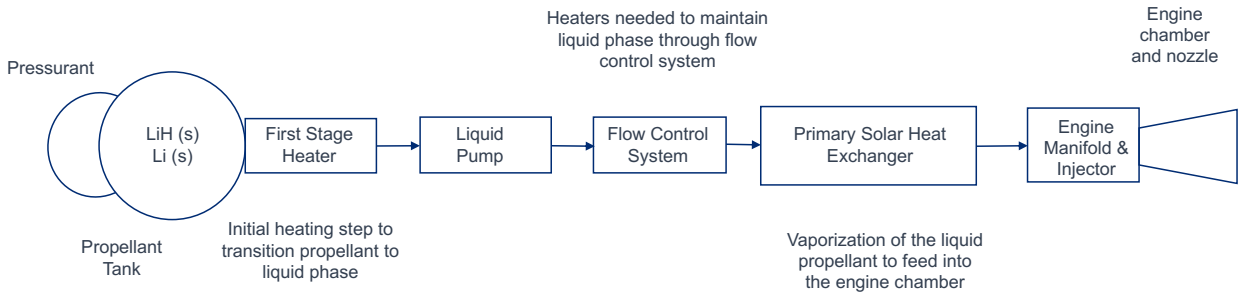

Figure 10. *Propulsion system mass evaluation for solid propellants, including lithium and lithium hydride.*

3.1.1.3. Lithium

The design for lithium followed that of lithium hydride insofar as it similarly required a first stage heater and pump owing to its high melting point (see Figure 10). The scaling of subsystem mass with lithium mass is given below.

Ti-6Al-4V: $m_{sub} = 0.1555 m_{Li} + 7 \times 10^{-14}$

304 Stainless Steel: $m_{sub} = 1.1821 m_{Li} - 2 \times 10^{-13}$

Al 7075: $m_{sub} = 0.1757 m_{Li} - 1 \times 10^{-13}$

3.1.1.4. Ammonia

The ammonia tank evaluation looked at material options and associated mass. Of all propellants, the ammonia storage system was perhaps the simplest (Figure 11). In terrestrial applications, ammonia is typically stored as a liquid under pressure (10 atm at 298 K) or refrigerated (1 atm at 240 K).[46] The fact that it requires neither thick walls for high pressure nor a vacuum shell for insulation results in the relatively favorable scaling relations shown below.

Ti-6Al-4V: $m_{sub} = 0.1394 m_{NH3} - 4 \times 10^{-14}$

304 Stainless Steel: $m_{sub} = 1.0599 m_{NH3}$

Al 7075: $m_{sub} = 0.1576 m_{NH3} - 2 \times 10^{-14}$

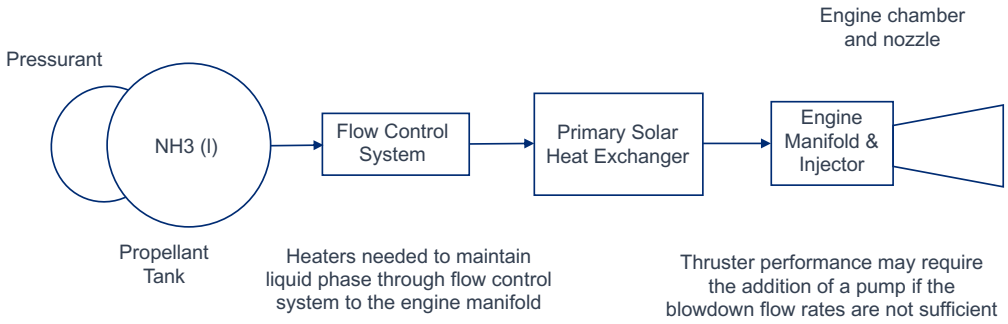

Figure 11. *The notional configuration for a storable liquid propellant such as ammonia.*

3.1.1.5. Methane

The storage of liquid methane incurs a larger penalty associated with cryogenic storage of the propellant (Figure 12). Gaseous methane was not included as the mass significantly exceeded any penalty associated with cryogenic storage. Considering the same three alloys as before, we arrive at the following scaling relations:

Ti-6Al-4V: $m_{sub} = 0.2047 m_{CH4} - 7 \times 10^{-14}$

304 Stainless Steel: $m_{sub} = 1.5565 m_{CH4} + 4 \times 10^{-13}$

Al 7075: $m_{sub} = 0.2314 m_{CH4} - 9 \times 10^{-14}$

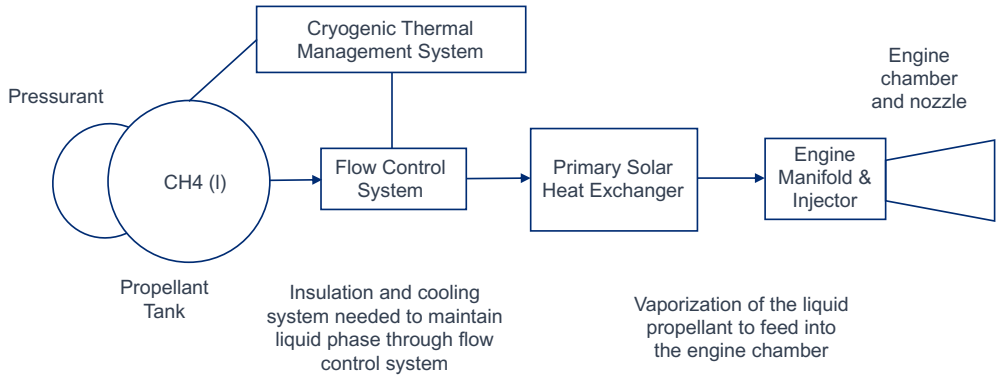

Figure 12. *Notional configuration for a cryogenic propellant option, such as liquid methane.*

3.1.1.6. Methane-Hydrogen Mixtures

The methane-hydrogen combined evaluation used 250 kg total propellant with the mass split between methane and hydrogen. Mass associated with a 1:4, 1:1, and 4:1 methane to hydrogen split were evaluated for titanium cases only. This case was a substantial mass increase over other propellant options so the stainless steel and aluminum tank options were not included. These tanks would include higher mass penalties since both propellants would require cryogenic storage. The mass associated with gaseous methane and hydrogen would not be credible.

The configuration for the notional cryogenic propellant blend subsystem is depicted in Figure 13 below. It should be immediately apparent that this approach has major disadvantages relative to either pure hydrogen or pure methane, both in complexity and mass. The mathematical scaling relationship between propellant mass and subsystem mass is provided for Ti-6Al-4V below.

Ti-6Al-4V: $m_{sub} = -1.0122 m_{CH4H2} + 304.23$

Given the extreme mass penalty incurred by the cryogenic propellant blend option, it is not considered for further analysis.

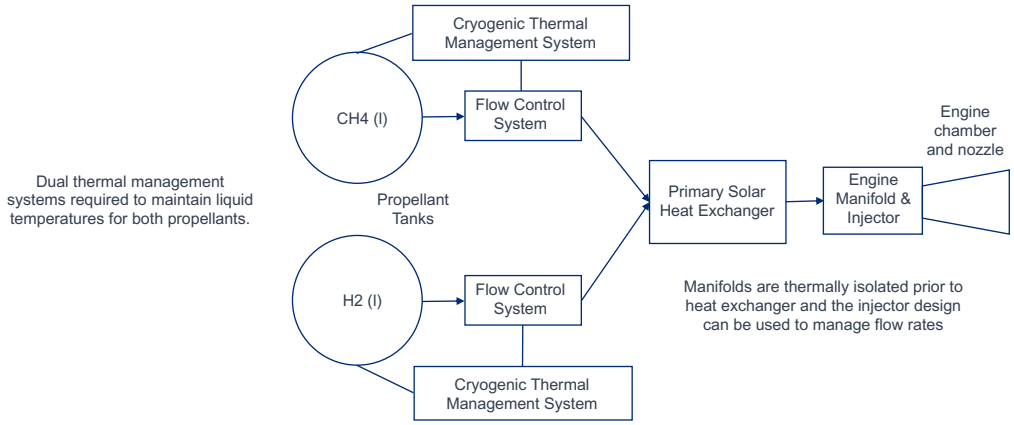

Figure 13. *Notional configuration for a cryogenic propellant blend option, liquid methane-liquid hydrogen.*

3.1.1.7. Propellant Storage and Handling Subsystem Mass Comparison

For the above scaling relations, we selected AlLi 8090 for hydrogen and Al 7075 for all others. Although Ti-6Al-4V provided marginally better mass performance, aluminum alloys were chosen to provide more conservative values for the subsystem dry mass. Figure 14 shows a comparison of how the tank mass scales with propellant mass for all propellants under consideration. The methane-hydrogen mixtures are excluded since that option was determined to be nonviable.

What becomes most clear from our analysis is that the two cryogenic options–hydrogen and methane–are significantly more massive than the others. Lithium and lithium hydride are solid at room temperature, so do not require pressurization. However, they do require additional heaters for propellant to be transported through the flow control subsystem as a fluid. Ammonia is especially intriguing, then, since it can be stored as a liquid without the need for cryogenic storage and requires only minimal heating to control its flow. Based on this mass analysis alone, one might expect that lithium, lithium hydride, and ammonia may be able to compensate for their lower specific impulse relative to hydrogen. Of these options, ammonia is perhaps the most conventional choice, carrying with it the lowest potential risk.

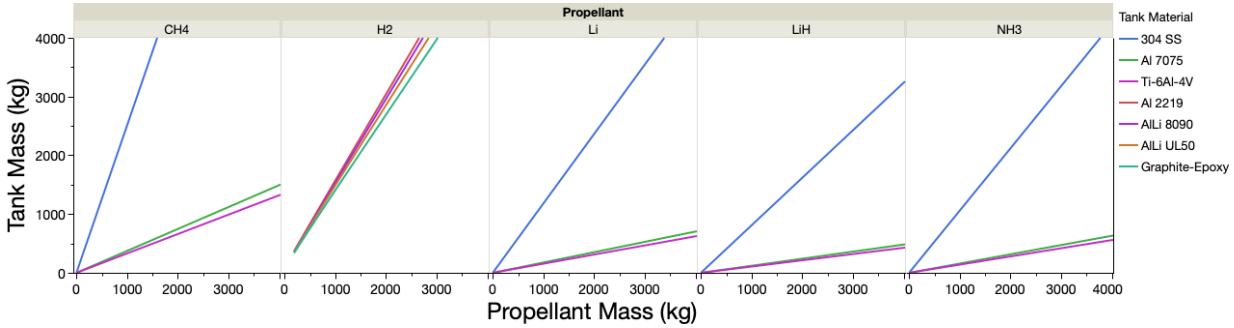

Figure 14. *Tank mass is plotted versus propellant mass for each tank material. Each panel represents a different propellant. Al 7075 was chosen for all propellants except hydrogen, which used AlLi 8090.*

3.1.2. Umbra Angle

The umbra angle (θ) is calculated from the geometrical relationship illustrated in Figure 15. It allows one to calculate the additional width on each side of the shield (Δw) that would be required to shadow an object of radius, r_{tank}. As shown below, the calculation further involves the radius of the Sun (R_s), distance to the Sun (r_p), payload standoff (h).

$$\frac{R_s}{r_{tank}} = \frac{r_p + x}{x}$$

$$\theta = atan\frac{R_s - r_{tank}}{r_p}$$

$$\Delta w = (R - r_{tank}) * \left(1 - \frac{d}{d + h + r_{tank}}\right)$$

If the tank radius is larger than the width of the spacecraft, then the width of the heat shield (W) needs to be

$$W = 2(r_{tank} + \Delta w)$$

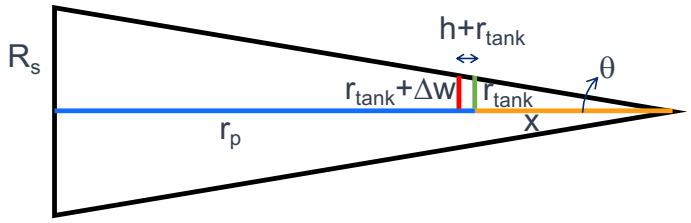

Figure 15. *Schematic illustration of the relationship between the umbra angle (θ) and the additional width (Δw) needed to shadow an object with radius, r_{tank}, placed a distance, h, behind the heat shield.*

The mathematical relationships show that the shield width is a function of the distance to the Sun. The mass penalty of the heat shield therefore increases with decreasing perihelion to some degree. The dependence of the umbra angle on the distance to the Sun in solar radii is presented in Figure 16.

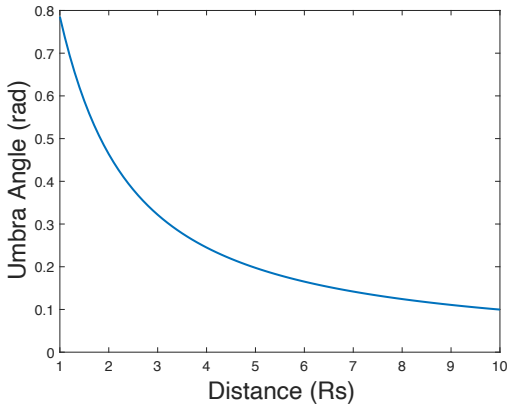

Figure 16. *The umbra angle is plotted as a function of distance from the Sun. The gap between the shield and spacecraft is fixed at 2.0 m.*

3.1.3. View Factor

The view factor from the back of the heat shield towards the bottom of the spacecraft bus determines the magnitude of radiative heat transfer. When the heat shield and spacecraft have the same dimensions and are positioned close together, the view factor is close to unity. If the heat shield is much wider than the spacecraft and there is a large standoff, then the view factor trends towards zero.

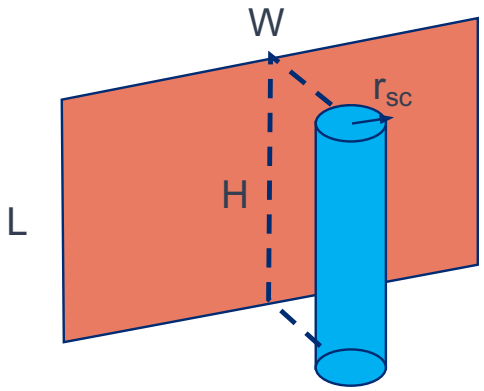

Figure 17. *Schematic of simplified geometry used to calculate the view factor from the heat shield to spacecraft*

In our analysis, we have approximated the payload as a cylinder with the same length as the heat shield. The radius of the cylinder (r_{sc}) is taken to be that of the New Horizons spacecraft. It is fixed at 1.05 m even if the propellant tank is larger than the spacecraft bus. The length of the cylinder (H) is taken to be the sum of the spacecraft bus (1.1 m), a deployable high gain antenna (1.9 m), small attitude controlling propulsion module (0.5 m), and propellant tank (variable). We further assume that the length of the heat shield (L) is equal to H. The width of the heat shield (W) is not equal to $2r_{sc}$, but rather the diameter of the propellant tank plus the correction for the umbra angle. The view factor (F) is then derived from the following relations[47]

$$X = \frac{H}{r_{sc}} \quad Y = \frac{W}{r_{sc}} \quad Z = \frac{L}{r_{sc}}$$

$$A = Z^2 + X^2 + \zeta^2 - 1$$

$$B = Z^2 - X^2 - \zeta^2 + 1$$

$$F = \frac{2}{Y}\int_0^{Y/2} f(\zeta)d\zeta$$

Consider how the spacecraft bus is nestled in a line with the propellant tank, antenna, and attitude control system. We can therefore justify the assumption of a cylinder with H = L on the basis that the adjacent subsystems shadow the front and back of the spacecraft. The radius of the cylinder (r_{sc}) is held equal to that of the spacecraft bus, because our primary constraint is based on the radiative heating of the spacecraft electronics. The view factor in the vicinity of the spacecraft bus is therefore more relevant to this constraint. A consequence of this supposition is that a larger propellant tank actually reduces the heating load on the spacecraft bus by necessitating a wider heat shield (larger W). Since the r_{sc} is constant, W/r_{sc} becomes greater than 1, and the view factor towards the spacecraft becomes smaller.

Figure 18 shows how the view factor decreases as a function of both payload standoff and tank radius. The payload standoff has a particularly pronounced effect. The spacecraft bus for Parker solar probe was approximately 2.0 m, so we used that value for our calculations unless otherwise noted. Taking that standoff, we see that the view factor drops to approximately 0.2 once the tank radius approaches 1.5 m. For reference, $2r_{sc}$ equals 2.1 m, so the tank–and heat shield–would be approximately one meter wider at that point. As will be shown in the following

section, the smaller view factor permits a reduction in the thickness of the heat shield.

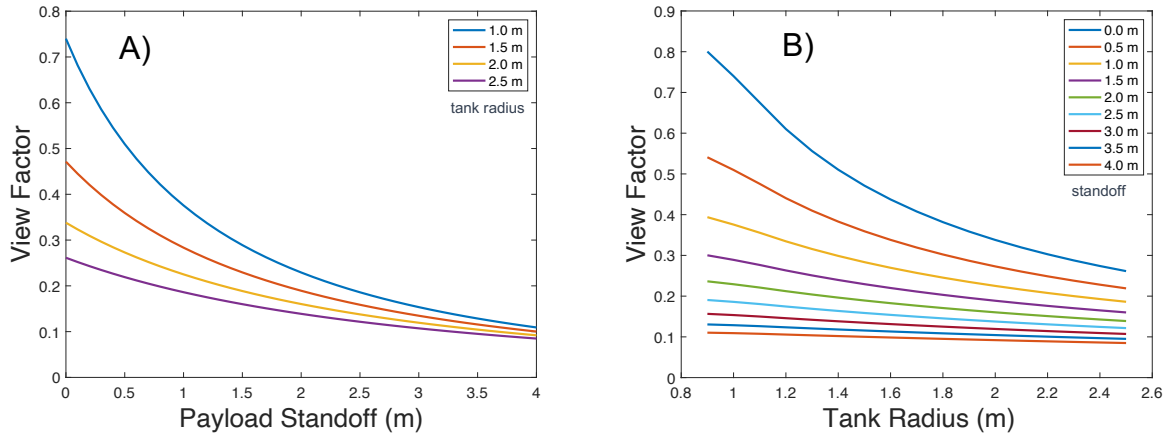

Figure 18. *A) The view factor from the back of the heat shield to the spacecraft is plotted as a function of payload standoff for each tank radius. B) The view factor is also plotted versus tank radius for each standoff.*

3.1.4. Shield Thickness

The shield thickness is governed by the thickness of the insulation that is required to stay below the maximum heat load on the bottom of the spacecraft bus. The pair of carbon composite face sheets on each side of the insulating layer have a roughly constant thickness determined by the mechanical loads during operation.

The maximum allowed heat flow to the spacecraft bus (J) is approximately 50 W. The effective emissivity of the spacecraft bus with MLI (ε*) is assumed to be 0.01, and the area of the spacecraft bus (A) is 2.1 m × 0.69 m = 1.45 m^2. These constraints combine to give the maximum allowed radiant exitance from the back of the heat shield (q).

$$q = \frac{J}{\varepsilon^* F A}$$

The next parameter that can now be addressed is the temperature of the back of the heat shield (T_{back}) that corresponds to this radiative heat flux. It follows from the Stefan-Boltzmann law that

$$T_{back} = \sqrt[4]{\frac{q}{\varepsilon\sigma}}$$

Here, σ is the Stefan-Boltzmann constant, and ε is the emissivity of the back of the heat shield, taken to be 0.8 for a carbon composite. So now finally we can derive an expression for the thickness of the heat shield (t) based on the temperature gradient ($\Delta T = T_{surface} - T_{back}$) and the thermal conductivity of the carbon foam insulation (k).

$$t = \frac{-k\Delta T}{q}$$

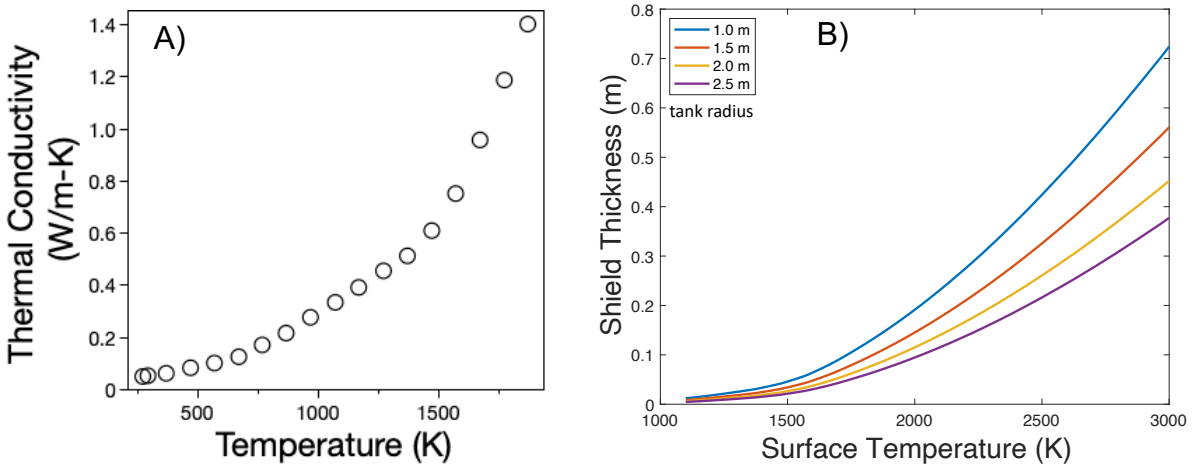

Figure 19. *A) The thermal conductivity of the carbon foam insulation from the Parker Solar Probe heat shield is plotted as a function of temperature. B) The shield thickness is plotted as a function of shield surface temperature. The different series correspond to different tank radii. The gap between the shield and spacecraft is fixed at 2.0 m.*

Unfortunately, k is an increasing function of temperature. Thermal conduction within the foam is dominated by radiative heat transfer at high temperatures. Figure 19A shows how sharply it rises for the type of insulating carbon foam used in the Parker Solar Probe heat shield. Observe how the slope increases above 1500 K. This raw data was extrapolated to higher temperatures in order to calculate the shield thickness for a given surface temperature, back side temperature, and view factor (Figure 19B).

In Figure 19B, we see a relationship that was alluded to in the previous section. The shield thickness that is necessary to keep the heat flux to the spacecraft bus below 50 W can decrease for a larger tank radius. When the tank has a 1.0 m radius, the shield and spacecraft bus have roughly equal widths. Going to larger tanks decreases the required insulation thickness because of the rapidly decreasing view factor from the shield to the spacecraft.

3.1.5. Shield Mass

The shield mass versus perihelion is calculated from the area and thickness by assuming a density (ρ) that is comparable to the Parker Solar Probe thermal protection system (PSP-TPS). That heat shield had a mass (m) of 72.7 kg, it had a 1.2 m radius (r_{PSP}), and the carbon composite was 0.115 m thick (t_{PSP}). If we take these terms together, then we obtain an average density of 140 kg/m^3.

$$\rho = \frac{m}{\pi r_{PSP}^2 t_{PSP}} = \frac{72.7}{\pi (1.2)^2 (0.115)} = 140\ kg/m^3$$

This is a somewhat rough approximation, because the carbon composite face sheets have a higher density than the carbon foam insulation. The true shield density is therefore not constant with thickness. Further differentiating the heat exchanger from the PSP-TPS is the inclusion of hollow tubes with a refractory metal lining. Together with density differences in the advanced carbon composites under current development, the average density of the heat exchanger should

remain close enough to 140 kg/m^3 to justify this approximation.

Figure 20 shows a contour plot of shield mass versus perihelion. We plot the range of values as a contour plot rather than the individual data points because of the large number of configurations. The surface temperature is a function of both the size of the tank and the size of the heat shield, each of which varied somewhat independently depending on the perihelion. Yet, for the most part, the shield mass had a nearly identical "hockey stick" shape for each propellant, rising rapidly below a perihelion of 5 R_s. Differences in the specific heat capacity and enthalpy of vaporization did not appear to have a significant effect on how the shield mass (via thickness) increased at smaller perihelions. We note here as well that propellants with higher density, such as liquid ammonia, will tend to decrease the shield area, because a given mass of propellant can be stored in a smaller tank.

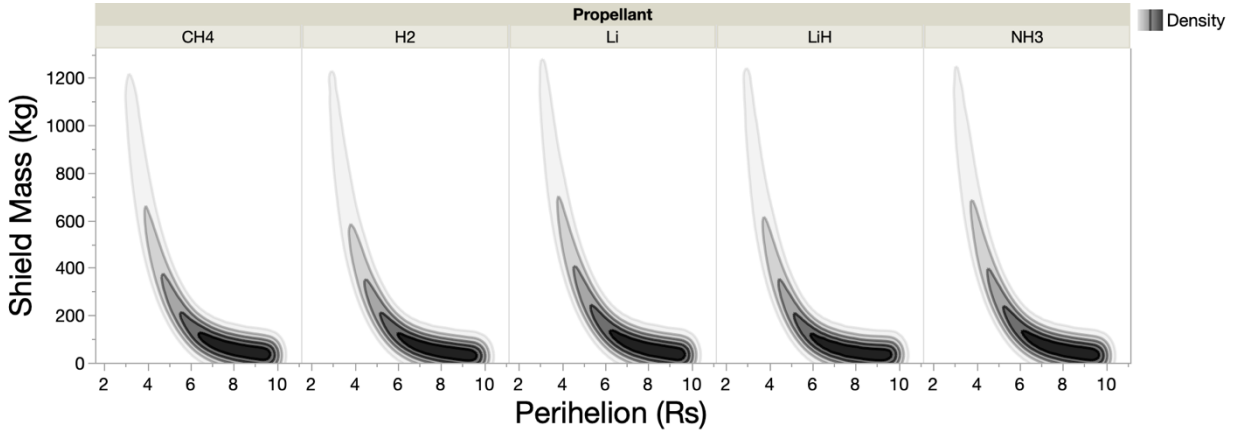

Figure 20. *A contour plot of shield mass versus perihelion is plotted for each propellant. The gap between the shield and spacecraft is fixed at 2.0 m.*

3.1.6. Total System Mass

The total system mass (wet mass) now becomes a straightforward sum of the spacecraft mass, shield mass, propellant mass, and propellant storage and handling system mass. The mass of the spacecraft includes instruments, accommodation hardware, telecommunications, guidance and control, power, thermal control, avionics, attitude control system, propulsion, mechanical, and harness. The APL study determined that an interstellar probe designed for a powered gravity assist around Jupiter would have an observatory dry mass of 661.6 kg,[38] and that value was used as a constant for this study. Only the propellant, heat shield, and propellant storage and handling system were allowed to vary in our calculations.

The total mass including propellant (wet mass) is shown in Figure 21 for each propellant as a function of shield temperature, perihelion and propellant fraction. Figure 22 shows the same for the dry mass (without propellant). They are depicted as contour plots in order to highlight trends and differences for the impact of each propellant on the system mass, independent of the specific impulse. Note that density in these plots refers to the number of configurations that had a given system mass for those input parameters.

The most obvious difference among the propellants is that increasing the quantity of hydrogen leads to a steep increase in system mass. Lithium, lithium hydride, and ammonia are almost the opposite. The dry mass is relatively insensitive to increasing amounts of these

propellants even up to a propellant fraction of 0.6.

Similar trends for lithium, lithium hydride, and ammonia are evident for the dry mass with respect to perihelion and shield temperature. While shield temperature is strongly coupled with decreasing perihelion, we see that the dry mass of the system remains relatively low even at small perihelion and high temperature. Methane and hydrogen, in contrast, show how the cryogenic storage tanks incur large mass penalties for virtually all temperatures and perihelions.

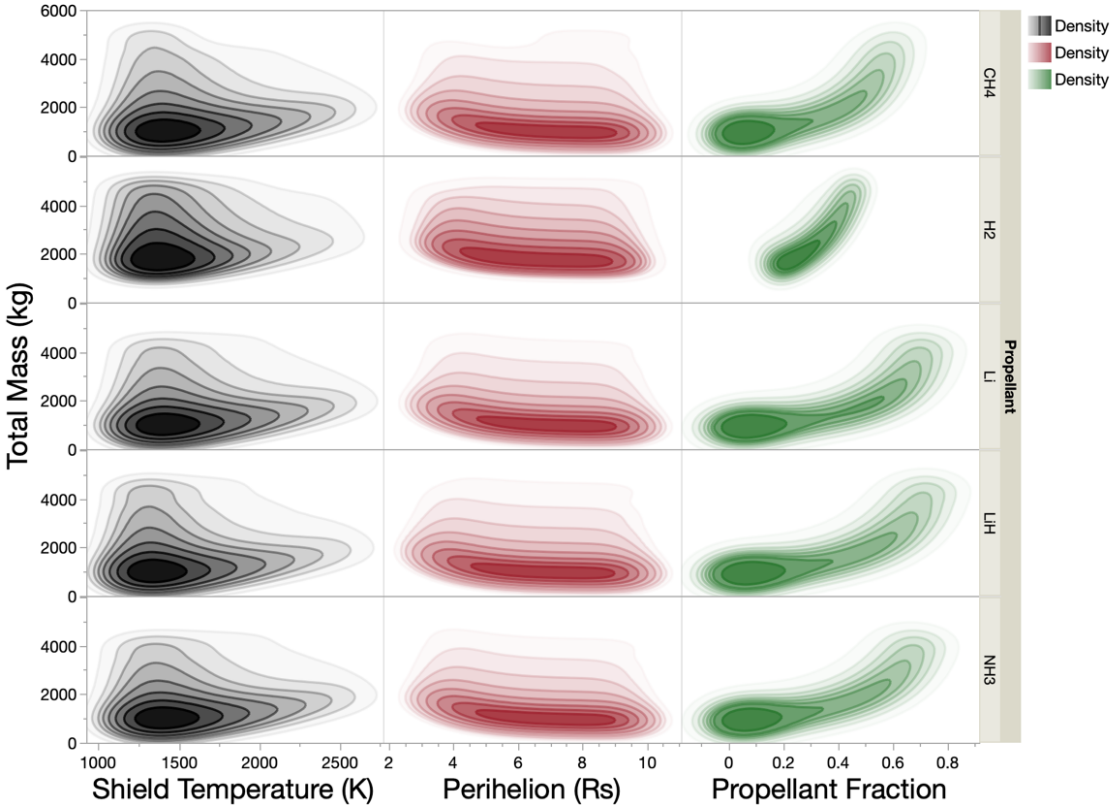

Figure 21. *Contour plots of total mass (wet mass) versus shield temperature, perihelion, and propellant fraction are plotted for each propellant. The maximum system mass is limited to 5000 kg, and the maximum surface temperature is limited to 2700 K.*

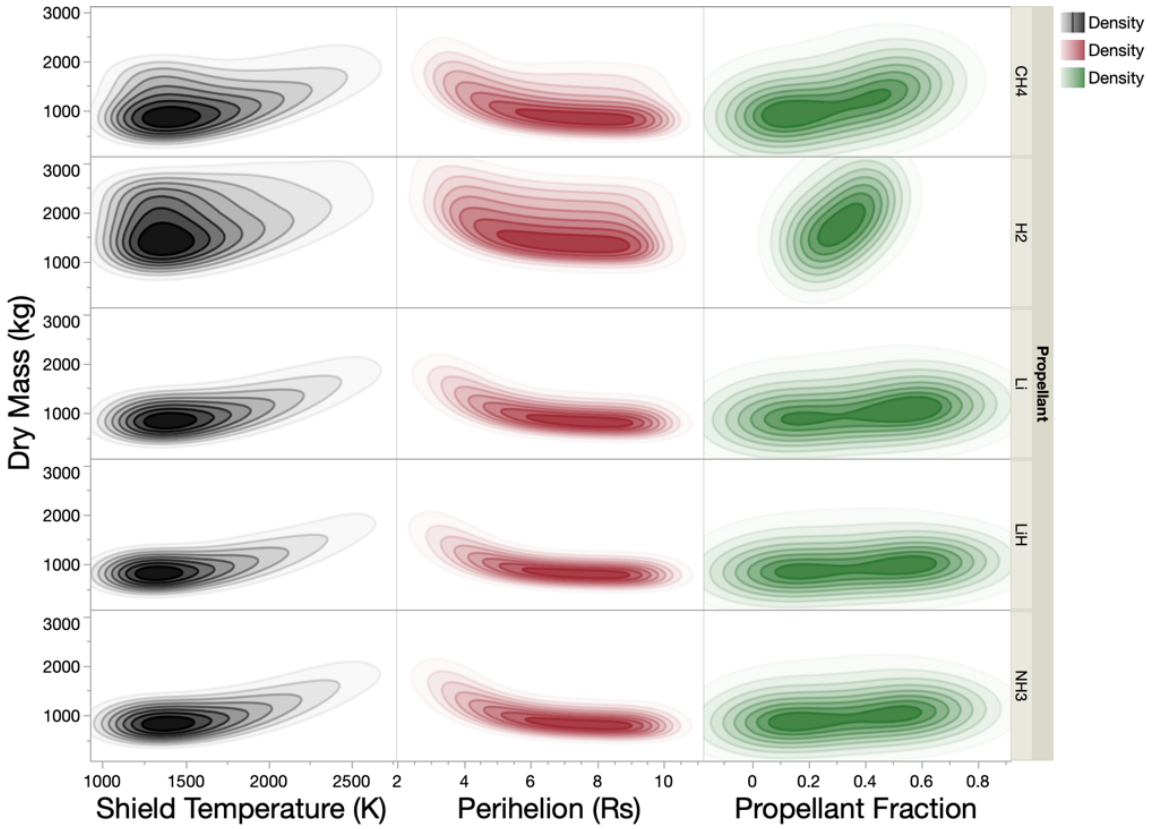

Figure 22. *Contour plots of dry mass versus shield temperature, perihelion, and propellant fraction are plotted for each propellant. The maximum system mass (wet mass) is limited to 5000 kg, and the maximum surface temperature is limited to 2700 K.*

The overall conclusion from looking at these trends is that the mass of the propellant storage handling system can dominate the dry mass of the system. It is particularly true when a massive cryogenic tank is required (methane and hydrogen). Three of the propellants with relatively simple storage systems–lithium, lithium hydride, and ammonia–had a dry mass and total system mass that only varied weakly with the amount of propellant and the type of trajectory. One would expect these propellants to therefore be amenable to designs with larger mass ratios (wet mass/dry mass) that can achieve a larger ΔV.

The mass ratio for each propellant is plotted as a function of perihelion in Figure 23. They are shown as contour plots to indicate the number of configurations for a given combination of mass ratio and perihelion. As expected, lithium, lithium hydride, and ammonia were able to achieve the highest mass ratios by far. Lithium hydride even exceeded a mass ratio of 4 within the constraints of having a maximum wet mass of 5000 kg and a maximum operating temperature of 2700 K. Hydrogen is at the other extreme. A few configurations had a mass ratio of 2, but these were generally at larger perihelions where the temperature, and thus specific impulse, is lower. Methane was not much better than hydrogen, only reaching a mass ratio of 2.75.

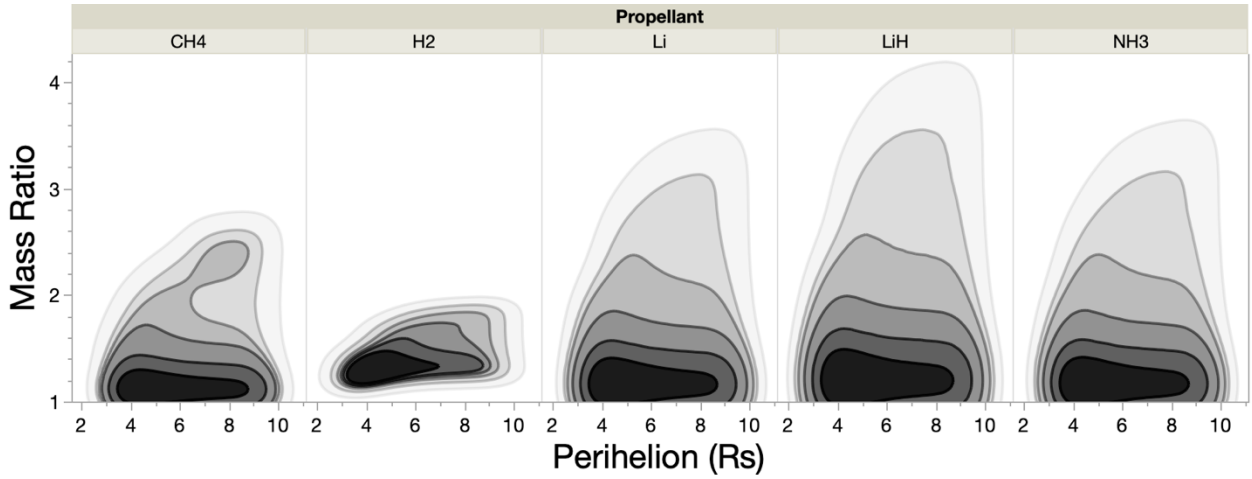

Figure 23. *The mass ratio is plotted as a function of perihelion for each propellant. The maximum system mass is limited to 5000 kg, and the maximum surface temperature is limited to 2700 K.*

3.1.7. Surface Temperature

3.1.7.1. Passive Thermal Control with Solar Selective Coating

Perhaps the largest opportunity for technological advancement over the PSP heat shield design is the alumina-based reflective coating. Aside from the need for a higher melting point, the optical properties can also be improved further to reduce the temperature for a given distance from the Sun. The equilibrium temperature of the coating is determined by the balance between the rate of sunlight absorption and the rate of blackbody radiation. The rate of sunlight absorption is proportional to the solar absorptance (α), and the rate of radiative cooling is proportional to the emissivity (ε). The steady state temperature occurs when both rates are equal. It is therefore crucial to minimize α/ε.

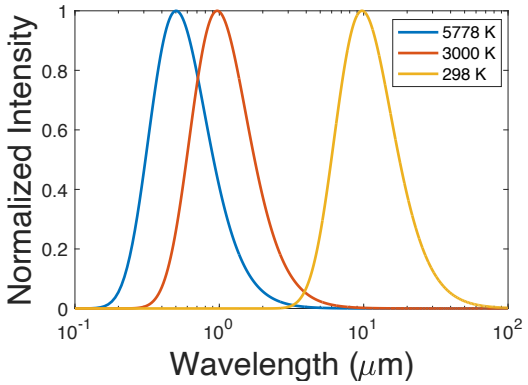

Figure 24. *Comparison of blackbody radiation to solar spectrum.*

The key to minimizing α/ε is to reflect strongly at shorter wavelengths where the solar irradiance (I_s) is largest and absorb strongly at longer wavelengths where the radiant exitance (I_r) is largest.[48] Unfortunately, the spectral radiance shifts to smaller wavelengths with increasing temperature.[49] The increasing overlap between I_s and I_r reduces the efficiency of cooling through

radiative heat loss. Figure 24 illustrates how the radiative output of a heat shield at 3000 K overlaps with the Sun at approximately 0.7 μm. It cannot emit blackbody radiation at its peak wavelength of 1 μm without absorbing the majority of near infrared light. Thus, the ability to regulate temperature with optical properties alone diminishes at high temperatures. Taking this argument to its logical extreme, α/ε converges to unity at 5778 K regardless of optical properties.

In this study, we adopted the optical properties of the solar-selective yttria-stabilized zirconia (YSZ) coating shown in Figure 25 A. Its reflectivity spectrum in Figure 25 B reveals a highly reflective surface with a solar absorptance of only 0.13. This compares to approximately 0.24 for the alumina-based coating on Parker Solar Probe. The YSZ coating therefore absorbs approximately half as much solar energy as the current best coating. Also note that the melting point of YSZ is about 2863 K, which is over 500 K higher than alumina, which melts at 2345 K.

The caveat to this improvement is that the new coating has not been exposed to the high temperatures and radiation environment experienced by the PSP heat shield. Any number of factors may increase the solar absorptance in this extreme environment, including the sintering of pores and cracks, Ostwald ripening of grains, changes in the optical constants, nonstoichiometric sublimation, redox reactions, and the formation of color centers.

For the purposes of our analysis, we will use the room temperature reflectance, but with the understanding that the optical properties are likely to degrade from the exposure to extreme temperatures and radiation. A fuller understanding of this degradation is beyond the scope of this study and will be reserved for future investigations. Some of these already under way are characterizing the changes in mass, composition, microstructure, and reflectance that result when oxide films are exposed to temperatures > 2000 K and vacuum. Early results suggest that oxide stability at low oxygen partial pressure will be key to surviving the approach to the Sun during a powered gravity assist.

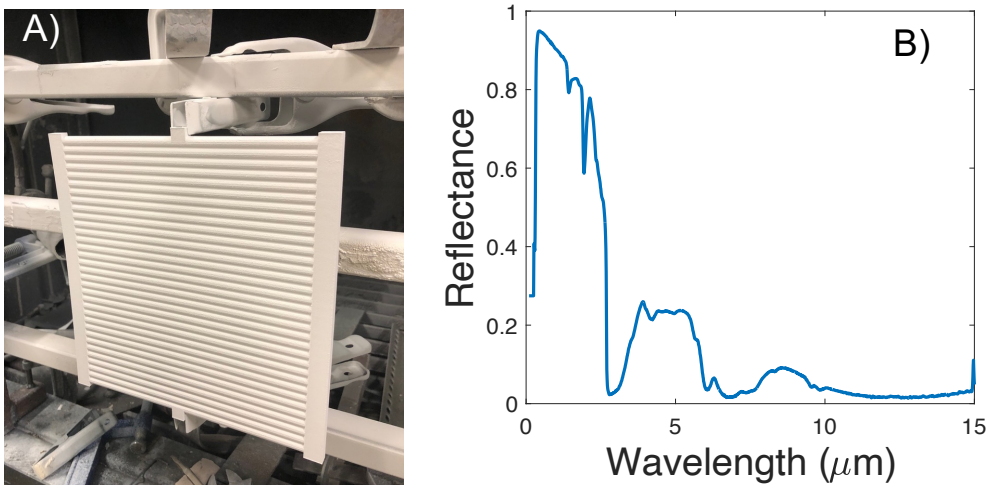

Figure 25. A) Prototype with yttria-stabilized zirconia coating. B) Its reflectance.

3.1.7.2. Contribution of Emissivity

At 1 AU (215 R_s), the Sun has a total irradiance (I_0) of 1377 W/m^2. The solar irradiance (I_s)

varies with r as:

$$I_s = I_0 \left(\frac{215}{r}\right)^2$$

The absorptivity is 1-R for opaque materials, where R is the reflectivity. The solar absorptance (α) is then defined as the weighted average of the absorptivity across the all wavelengths (λ).

$$\alpha = \frac{\int_0^\infty [1 - R(\lambda)] I_s(\lambda) d\lambda}{\int_0^\infty I_s(\lambda) d\lambda}$$

The rate of energy absorbed by the heat shield due to absorption of the solar irradiance (P_{sun}) is therefore

$$P_{sun} = \alpha I_s = \alpha I_0 \left(\frac{215}{r}\right)^2$$

According to the Stefan-Boltzmann law,[50, 51] the radiant exitance from a blackbody (I_r) scales with the fourth power of temperature (T). Much like the absorption of sunlight, radiative emission is only a fraction of the total possible blackbody radiation, defined as the emissivity (ε). Kirchhoff's law states that the emissivity and absorptivity are identical for bodies emitting and absorbing thermal radiation in thermodynamic equilibrium. Thus, we similarly define the emissivity as the weighted average of the absorptivity over the spectral radiance of the blackbody ($I_r(\lambda,T)$).

$$\varepsilon = \frac{\int_0^\infty [1 - R(\lambda, T)] I_r(\lambda, T) d\lambda}{\int_0^\infty I_r(\lambda, T) d\lambda}$$

Here the spectral radiance of the blackbody as a function of wavelength and temperature (I_r) is given by Planck's law[52]

$$I_r(\lambda, T) = \frac{8\pi hc^2}{\lambda^5} \frac{1}{exp[hc/(\lambda k_B T)] - 1}$$

where h is Planck's constant, k_B is Boltzmann's constant, and c is the speed of light. It therefore follows that the rate of energy emitted from the heat shield is

$$P_{rad} = \varepsilon \, \sigma T^4$$

Setting $P_{sun} = P_{rad}$, and solving for T gives the following expression for the equilibrium temperature.

$$T = \sqrt[4]{\frac{215^2 \alpha I_0}{\varepsilon \sigma r^2}}$$

3.1.7.3. Contribution of Active Cooling

A solar Oberth maneuver consists of three stages. The first is a Hohmann transfer from Earth to Jupiter. After a gravity assist, the spacecraft is redirected towards the Sun on a hyperbolic trajectory. At the perihelion the spacecraft performs a powered gravity assist and then travels

outward on another hyperbolic trajectory, but with a greater escape velocity. For the purposes of this discussion, we focus on the incoming and outgoing hyperbolic trajectories around the Sun. These provide the distance from the Sun as a function of time, and therefore the temperature as a function of time. We will then show how a variable flow rate of hydrogen can minimize the temperature by keeping it constant during the Oberth maneuver.

The trajectory of the Oberth maneuver is derived from the vis-viva equation

$$r = \frac{a(1-e^2)}{1+e\cos\theta}$$

where a is the semi-major axis, e is the eccentricity, and θ is the angular coordinate. We approximate the approach and return as a hyperbolic trajectory. The semi-major axis is a function of the hyperbolic excess velocity at infinite distance (v_∞), the gravitational constant (G = 6.67 x 10^{-11} m^3/kg-s^2), and the mass of the Sun (M = 1.99 x 10^{30} kg).

$$a = -\frac{GM}{v_\infty^2}$$

The eccentricity is a function of the perihelion (r_p) and a.

$$e = -\frac{r_p}{a+1}$$

From above, one can see that the only difference between the incoming and outgoing trajectories is the value of v_∞. The outgoing hyperbolic excess velocity is taken to be 15 AU/yr. This corresponds to a perihelion of 2.5 R_s and a mass ratio of 2.

The excess velocity for the incoming trajectory requires a different set of assumptions. It is determined by the unpowered gravity assist at Jupiter. The calculation was performed according to the method of McNutt, et al.[53] First, the Hohmann transfer orbit was calculated from Earth (r_E = 1.5 × 10^8 km) to Jupiter (r_j = 7.8 × 10^8 km). A C_3 value of 165 km^2/s^2 for an SLS rocket using the iCPS is assumed. Next, the increase in velocity was calculated for a trajectory in which the outgoing angle from Jupiter coincided with the incoming hyperbolic trajectory at the same velocity and distance. For an angle of 1.08 radians with respect to the orbital velocity vector of Jupiter in the heliocentric frame, one obtains a velocity of 12.4 km/s. This velocity (v_a) is then related to the incoming hyperbolic excess velocity ($v_{\infty in}$) as follows.

$$v_{\infty in} = \left(v_a^2 - \frac{2GM}{r_j}\right)^{0.5}$$

Thus, the Oberth maneuver is modeled as a hyperbolic trajectory with an incoming velocity of 17.7 km/s (3.7 AU/yr) at infinite distance, and an outgoing velocity of 71.2 km/s (15 AU/yr). The full trajectory is shown in Figure 26 A. The distance from the Sun is plotted as a function of time in Figure 26 B. Note how the maneuver takes a little over two years to complete.

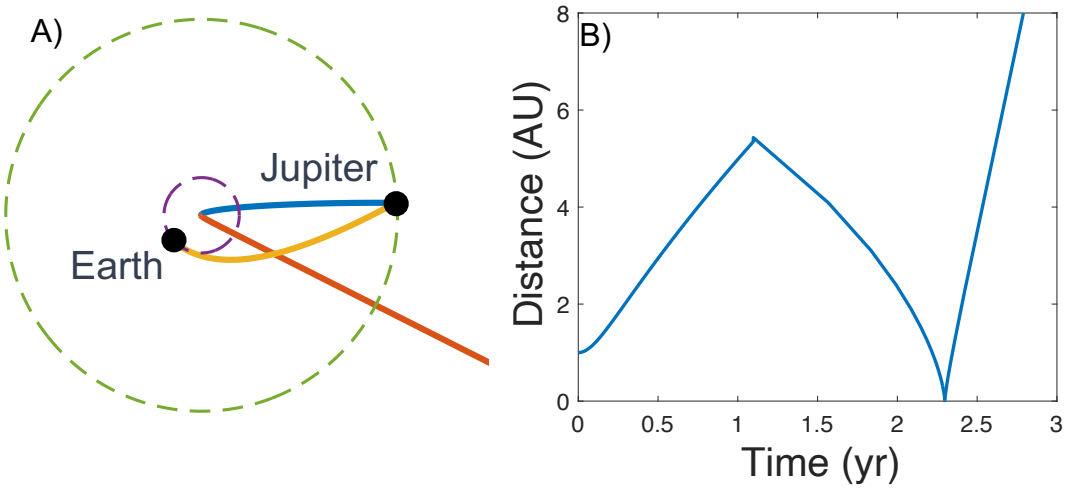

Figure 26. *A) Trajectory of the Oberth maneuver for 500 kg payload and C_3 165 km²/s². B) Distance from Sun versus time.*

With distance known as a function of time, it is now possible to calculate the temperature as a function of time. The result is plotted in Figure 27 A for a perihelion of 2.5 R_s. Over the course of 6 hours, the temperature of the front surface of the heat shield increases from 1500 to 3000 K. The temperature drop on the outgoing leg is slightly faster due to the ΔV at the perihelion. Regardless, the key feature is the constant temperature created by the variable flow rate. In these calculations, we assumed that the heat shield had a total area of 6 m². The flow rate was allowed to vary such that the total expended quantity was 500 kg (Figure 16 B).

Figure 16 C shows that the change in temperature is more gradual for a perihelion of 4 R_s. While the maximum temperature is lower, the spacecraft spends a longer time at elevated temperature because of the decreased speed with increasing perihelion. Accordingly, the same 500 kg of hydrogen is expended for a longer time and at a lower peak mass flow rate.

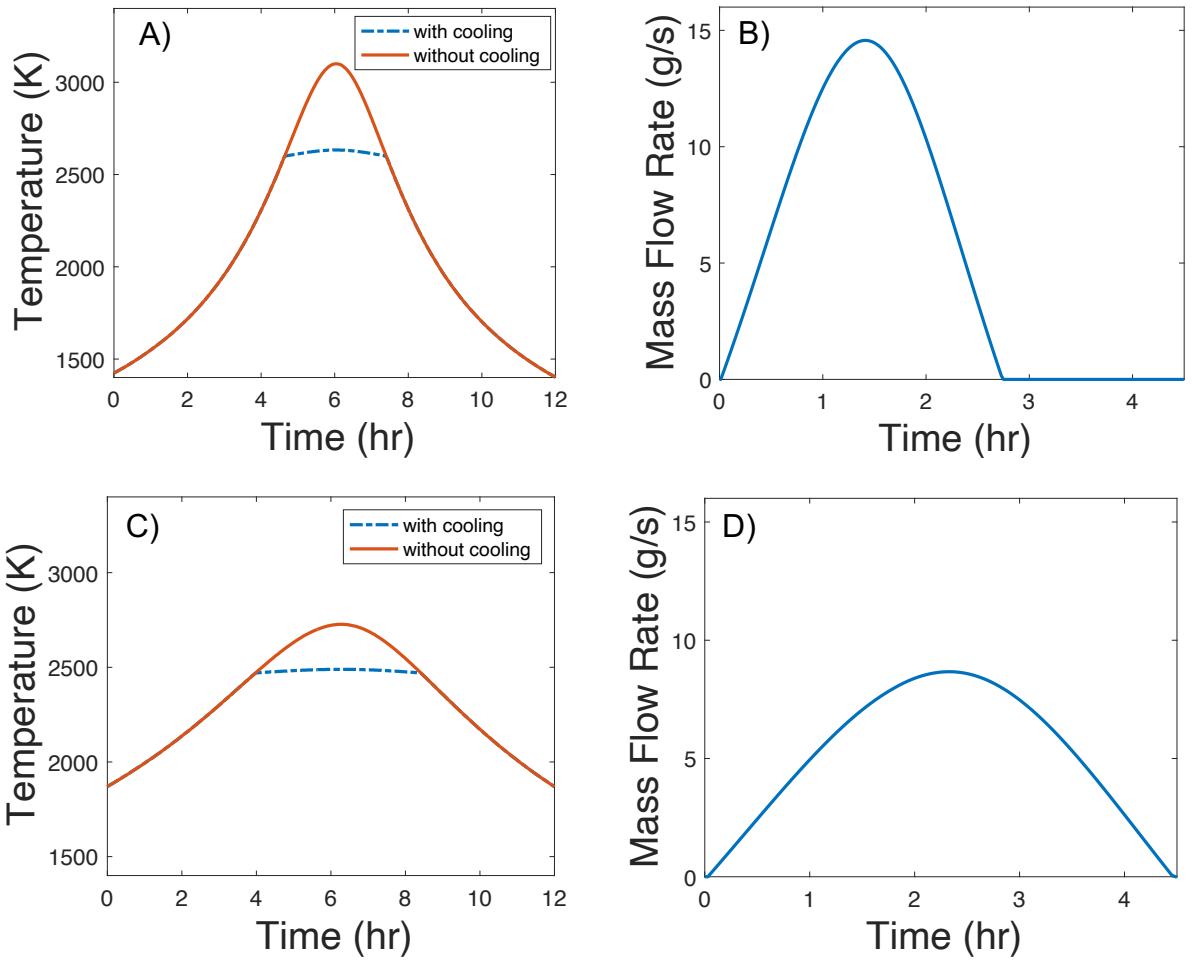

Figure 27. *A) Heat shield temperature with and without H_2 cooling at 2.5 R_s. B) Flow rate as a function of time at 2.5 R_s. C) Heat shield temperature with and without H_2 cooling at 4 R_s. D) Flow rate as a function of time at 4 R_s.*

It is instructive to show why a constant burn rate is not desirable. We can consider a much shorter impulse of 30 minutes for the same trajectory (Figure 28). For a 6 m^2 shield and a total H_2 mass of 500 kg, the flow rate increases to 46 g/m^2-s. Here the temperature drop is 850 K. Counterintuitively, the maximum temperature is actually higher than for the variable rate hydrogen burn. It is only 42 K lower than the temperature with no hydrogen at all. On each side of the 30-minute burn, the shield exceeds 3000 K, well above the melting point of YSZ. Furthermore, the specific impulse is actually lower due to the extreme cooling caused by the faster hydrogen flow rate. The burn occurs at 1820 K, 1180 K lower than the temperature without hydrogen cooling and 811 K lower than the temperature with a variable flow rate. At 2631 K, the specific impulse is about 900 s, while at 1820 K, it drops all the way down to 750 s. Thus, the variable flow rate improves both survivability and ΔV.

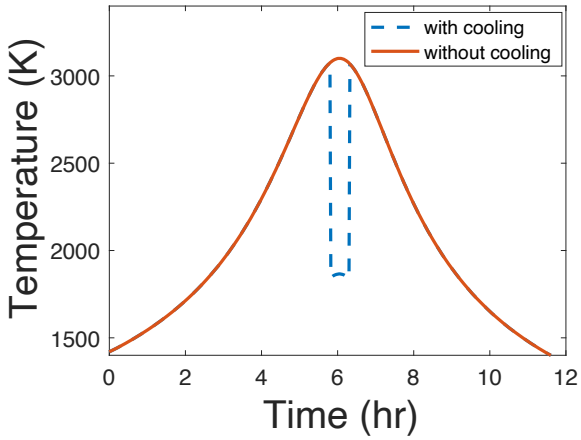

Figure 28. *A) Surface temperature for a 30-minute burn with 500 kg of H_2 at a constant rate of 46 g/m^2-s.*

To evaluate the cooling effects of each propellant, we compiled the density, boiling point, heat of vaporization, and specific heat capacity. Specific heat values were chosen for 2000 K when possible, or the closest temperature that was available in the dataset. The properties that were used for the calculations are listed in Table 2 below.

Table 2. Propellant properties used for active cooling calculations

Propellant	**Molar Mass**	**Specific Heat (J/g-K)**	**Liquid Density (kg/m^3)**	**Boiling Point (K)**	**Heat of Vaporization (J/g)**
Hydrogen	2.016	14.32	70	20	461
Methane	16.04	2.23	423	112	509
Lithium	6.941	3.00	512	1615	21192
Lithium Hydride	7.95	4.84	580	1220	27157
Ammonia	17.03	2.94	817	240	1372

3.1.8. Specific Impulse

NASA's Chemical Equilibrium Applications (CEA) program was used in rocket mode to evaluate theoretical performance of a solar powered rocket for an Oberth maneuver using different propellants. The propellants evaluated are H_2, Li, LiH, NH_3, CH_4, and three H_2-CH_4 mixtures. H_2O was also considered so the authors could compare results to existing literature, however, H_2O was not considered within the overall system engineering trade study. CEA is able to model chemical rocket combustion and theoretical nozzle performance for a set of propellants given rocket chamber, throat, and nozzle constraints. Combustion is not considered for this use as the propellant is heated by the Sun's energy for solar powered propulsion. Therefore, no

oxidizer is needed. Two operation modes for rockets can be used, equilibrium and frozen. For equilibrium the propellant is allowed to come to chemical equilibrium at each solution point. For frozen the chemical makeup of the solution is frozen at a chosen point and no reactions are allowed to take place after that point. The solution can be frozen at the chamber, throat, or exit.

Outputs from CEA were the vacuum specific impulse (I_{sp}) for both equilibrium and frozen at the combustion chamber solutions. CEA was run assuming an infinite combustion chamber and an exit to throat area ratio of 60. Although larger area ratios would increase performance, the relative performance between propellants does not vary so running at other area ratios is not necessary. True area ratio will be constrained by mass and thermal shielding considerations. Chamber pressures were set to be 0.69, 5.17, and 13.8 bar while chamber temperature was varied to be between 2000 and 3500K except for Li, which started at 2200K as the exit temperature was below the condensation point for Li otherwise even in equilibrium mode.

This problem for Li was present for other propellants in frozen flow mode. (Specifically the error message is: " WARNING!! CALCULATIONS WERE STOPPED BECAUSE NEXT POINT IS MORE THAN 50 K BELOW THE TEMPERATURE RANGE OF A CONDENSED SPECIES (ROCKET)") The problem is caused by some of the material/s in the flow that are cold enough to condense to a liquid, invalidating the frozen solution. This was encountered for Li at low chamber temperatures for both equilibrium and frozen solutions and CH_4 for low temperature frozen solutions. Lowering the expansion ratio can fix this error.

The results for each propellant are provided in Figure 29, Figure 30, Figure 31. The figures represent a chamber pressure of 0.69 bar, 5.17 bar, and 13.8 bar, respectively. The specific impulse corresponding to highest chamber pressure was selected for our subsequent calculations in order to provide a more conservative value for ΔV and the escape velocity. It is unclear what pressures will be required to drive the mass flow rates during the Oberth maneuver. Figure 2 predicts that they could exceed 30 g/s of propellant per square meter of heat shield. Depending on the diameter of the tubing, the length of the tubing, and the area of the heat shield, the pressure could potentially be high, but a value of 13.8 bar is probably sufficient to encompass most configurations that would account for the burst strength of the carbon composite tubes at temperatures exceeding 2000 K.

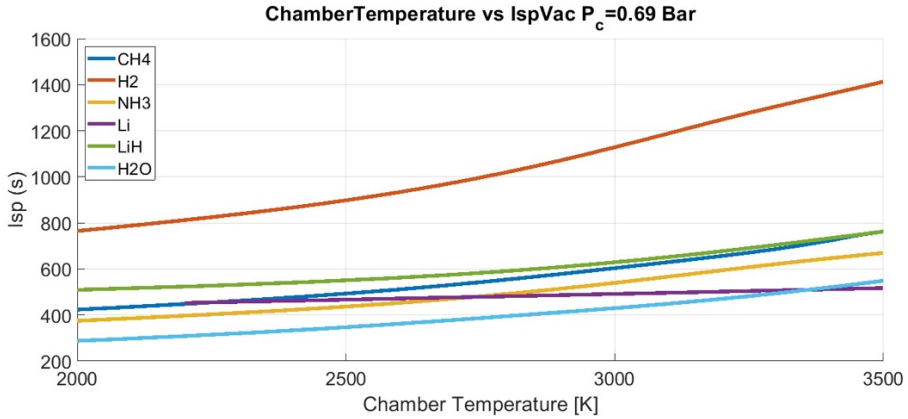

Figure 29. *I_{SP} for the propellants at 0.69 bar.*

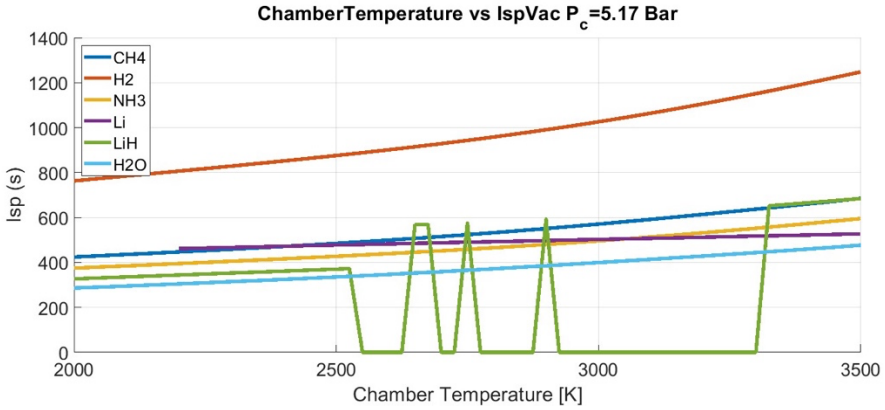

Figure 30. *I_{SP} for the propellants at 5.17 bar.*

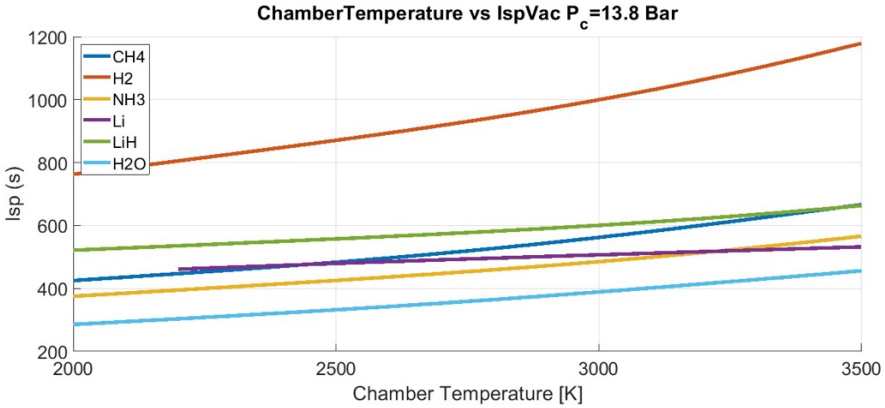

Figure 31. *I_{SP} for the propellants at 13.8 bar.*

An additional set of propellants that were considered were mixes of H_2 and CH_4. As show in Figure 32, the results are distributed based on amount of H_2 content, more H_2 leads to a higher I_{sp}. This is as expected.

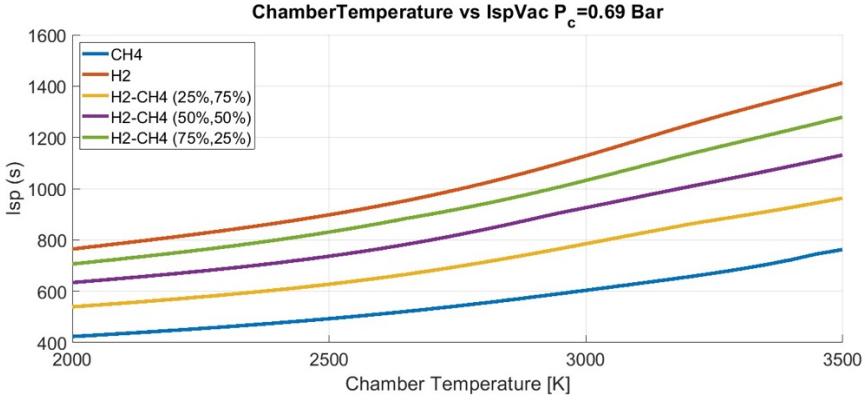

Figure 32. *I_{SP} for the H_2-CH_4 mixtures at 0.69 bar.*

3.1.9. Escape Velocity

The escape velocity (V_{esc}) is calculated from the change in velocity (ΔV) and perihelion (r_p) using

the following equation:

$$V_{esc} = \frac{7.4142\Delta V^{1/2}}{r_p^{1/4}}$$

ΔV, in turn, is calculated by knowing the acceleration of gravity (g_0), specific impulse (I_{sp}) and mass ratio (m_r), defined as the wet mass (m_0) divided by the dry mass (m_f). It is given by the Tsiolkovsky rocket equation:

$$\Delta V = g_0 I_{sp} \ln\left(\frac{m_0}{m_f}\right)$$

One can now appreciate the large number of steps that were required to calculate the mass ratio. In the previous sections, we saw that the dry mass is a function of perihelion, because both the area and thickness of the shield increase as one gets closer to the Sun. We also observed that the dry mass is a function of the quantity of propellant, because the size of the tank and area of the heat shield had to grow.

The other complication in these calculations is that the temperature of the heat shield at a given perihelion has a complex dependence on the quantity of propellant. The overall trend is that the specific impulse decreases with increasing mass ratio for a given perihelion. The reason for this trend is that the mass of propellant normalized to the area of the heat shield determines the magnitude of active cooling that is possible during the Oberth maneuver. This dependence is not straightforward, because a larger tank requires a larger shield area. Furthermore, the shield area increases with decreasing perihelion. Taken together, a long series of calculations is required to determine the temperature for each propellant, at each perihelion, and each mass ratio.

3.1.9.1. Hydrogen

Under a previous set of assumptions that were more favorable to hydrogen, we calculated an escape velocity of 10.7 AU/yr at a perihelion of 4 R_s (Figure 2B). The primary difference was the selection of a carbon fiber-epoxy composite tank. That calculation also did not account for the maximum operating temperature of the heat shield. All masses and all trajectories were included in the calculation, with the only constraint being the total payload of 5000 kg.

To arrive at a more fair estimate of the escape velocity from the solar system, it was recalculated by assuming that the propellant tank was constructed from AlLi 8090 alloy. This alloy is currently available in sufficient quantity for the tank sizes under consideration here. It is also a more direct comparison with the Al 7075 alloy that was selected for all other propellant storage systems. In general, Ti-6Al-4V performed better on a mass basis, but the difference was small. Aluminum was therefore a more conservative choice that would yield a more realistic estimate for the escape velocity that could be achieved using a combined heat shield and solar thermal propulsion system.

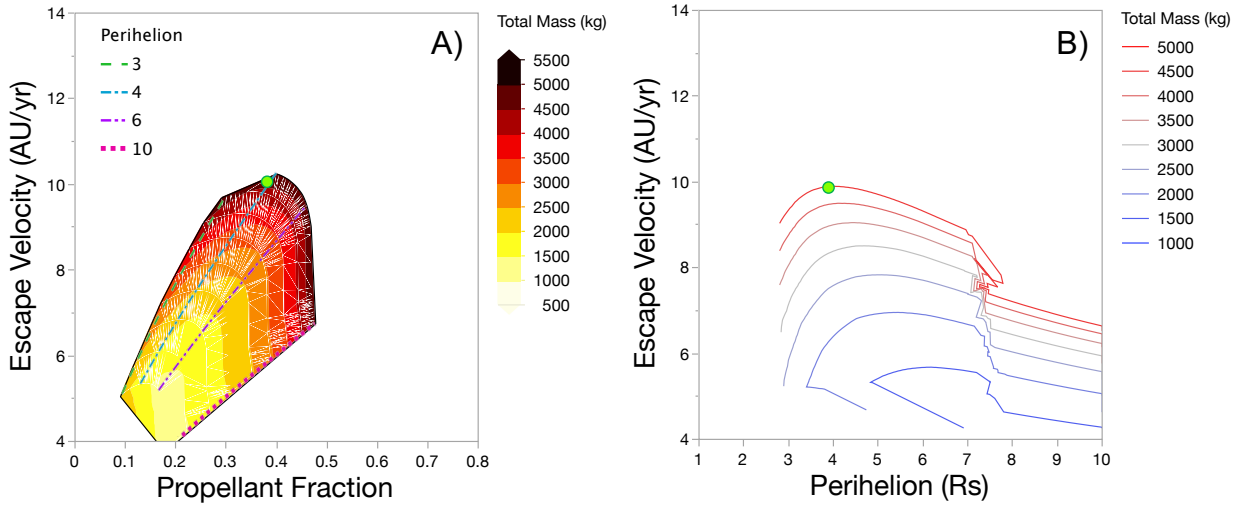

Figure 33. *A) The escape velocity is plotted versus propellant fraction for hydrogen for different perihelions ranging from 3 to 10 R_s. The heat map behind the plots displays the total system mass that corresponds to the given escape velocity. B) The escape velocity is plotted versus perihelion for different total system masses, ranging from 1000 kg to 5000 kg. The maximum system mass is limited to 5000 kg, and the maximum surface temperature is limited to 2700 K. The green dot identifies the maximum escape velocity of 9.9 AU/yr at a perihelion of 4.0 R_s.*

The results of the calculations are presented in Figure 33. Figure 33A shows the escape velocity as a function of propellant fractions for different perihelions. A contour plot of the total system mass (wet mass) is overlaid on the data to indicate how the wet mass and propellant fraction increase in relation to each other. Only shown are configurations and trajectories that have a total system mass below 5000 kg and a maximum operating temperature less than 2700 K, which is the melting point of the yttrium oxide coating. Figure 33B shows the escape velocity as a function of perihelion for different total system masses ranging from 1000 kg to 5000 kg. One can see something of a diminishing return for increasing the system mass beyond 4500 kg.

The adjustments made to the hydrogen calculations reduced the predicted escape velocity from 10.7 AU/yr down to 9.9 AU/yr. The optimal perihelion remained at 4.0 R_s. This velocity is still much greater than the value of 7.2 AU/yr that was estimated for an SLS rocket performing a passive gravity assist around Jupiter. That said, the extra risk and expense to develop this unconventional system would only produce a 37% increase in the escape velocity under these assumptions. In order for hydrogen to be a viable propellant for this approach, lighter cryogenic storage tanks must be developed, either through improved materials, such as carbon fiber-epoxy composites, or through other mass-saving designs.

3.1.9.1. Lithium Hydride

The escape velocity of lithium hydride is shown as a function of propellant fraction in Figure 34A, and as a function of perihelion in Figure 34B. We find a maximum escape velocity of 12.3 AU/yr at a perihelion of 4.5 R_s. It is the largest predicted escape velocity of all propellants and 1.7x faster than a passive gravity assist around Jupiter with an SLS rocket. The relatively low mass of the propellant storage and handling system manifests itself in the relatively large

propellant fraction that can be achieved while remaining within the 5000 kg payload limit. Observe how some configurations are over 70% lithium hydride by mass. It is enough to compensate for the somewhat lower specific impulse to the extent that its escape velocity is 1.24x faster than hydrogen.

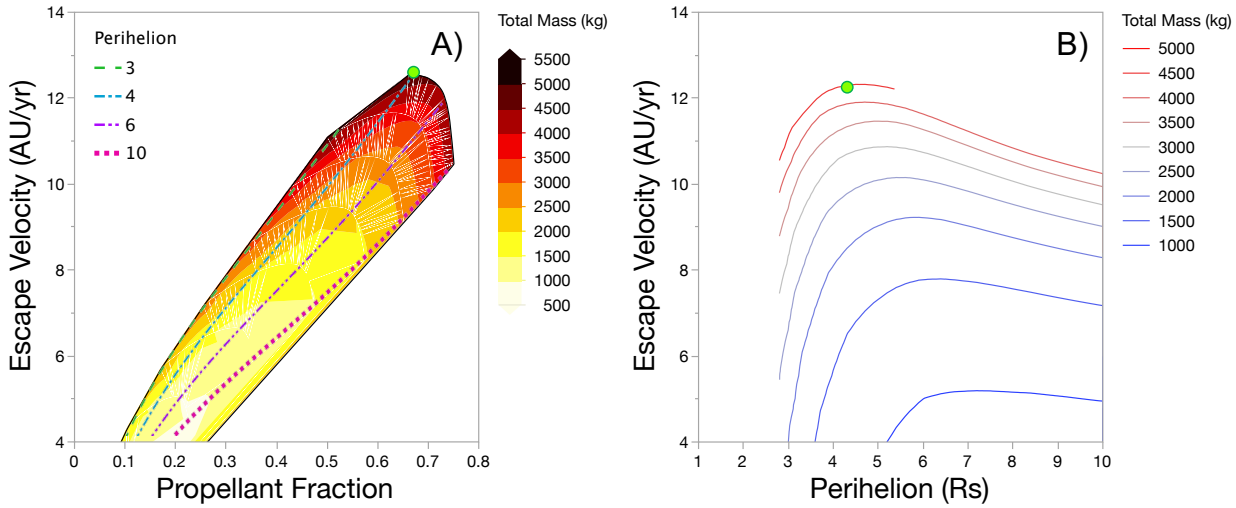

Figure 34. *A) The escape velocity is plotted versus propellant fraction for lithium hydride for different perihelions ranging from 3 to 10 R_s. The heat map behind the plots displays the total system mass that corresponds to the given escape velocity. B) The escape velocity is plotted versus perihelion for different total system masses, ranging from 1000 kg to 5000 kg. The maximum system mass is limited to 5000 kg, and the maximum surface temperature is limited to 2700 K. The green dot identifies the maximum escape velocity of 12.3 AU/yr at a perihelion of 4.5 R_s.*

3.1.9.1. Lithium

The escape velocity of lithium is shown as a function of propellant fraction in Figure 35A, and as a function of perihelion in Figure 35B. Lithium has much in common with lithium hydride in terms of both being stored as solids and both having similar molar masses. However, the analysis of the propellant storage and handling system suggests that the subsystem mass penalty is slightly higher for lithium. It still has a greater escape velocity than hydrogen, estimated at 10.7 AU/yr at a perihelion of 4.7 R_s.

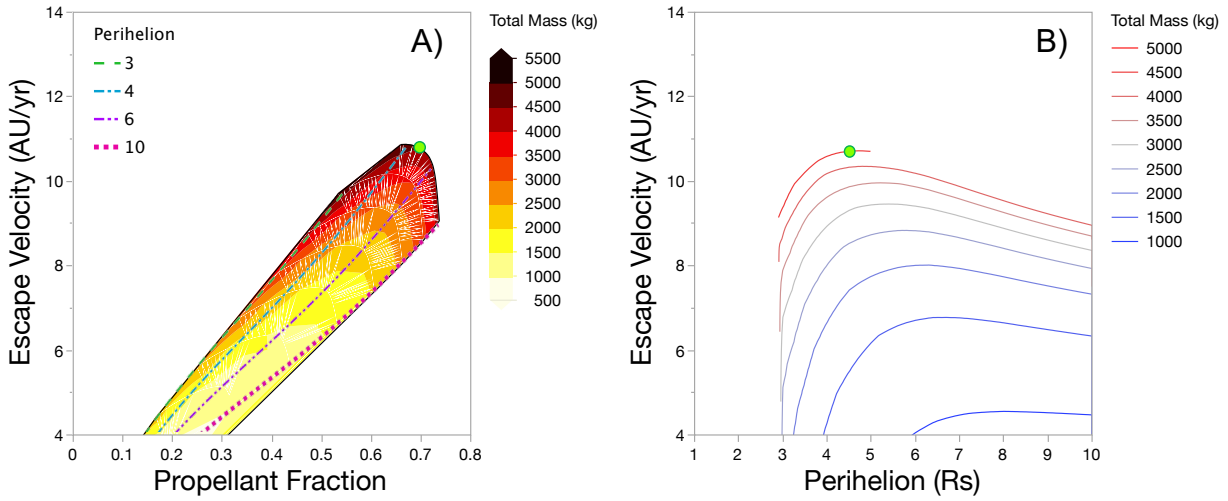

Figure 35. *A) The escape velocity is plotted versus propellant fraction for lithium for different perihelions ranging from 3 to 10 R_s. The heat map behind the plots displays the total system mass that corresponds to the given escape velocity. B) The escape velocity is plotted versus perihelion for different total system masses, ranging from 1000 kg to 5000 kg. The maximum system mass is limited to 5000 kg, and the maximum surface temperature is limited to 2700 K. The green dot identifies the maximum escape velocity of 10.7 AU/yr at a perihelion of 4.7 R_s.*

3.1.9.1. Ammonia

The other intriguing propellant from this trade study is ammonia. Ammonia can be stored as a liquid without the need for high pressurization or cryogenic storage. Its propellant storage and handling system therefore incurs the smallest mass penalty and the smallest risk. We see the results for the escape velocity as a function of propellant fraction in Figure 36A, and the escape velocity as a function of perihelion in Figure 36B.

Much like lithium and lithium hydride, the plot in Figure 36A includes configurations that reach far to the right on the plot. It, too, can achieve propellant fractions greater than 0.7 while remaining within the 5000 kg limit. Thus, at a perihelion of 4.2 R_s, it can reach an escape velocity of 10.0 AU/yr. While not as high as lithium or lithium hydride, it is still greater than hydrogen.

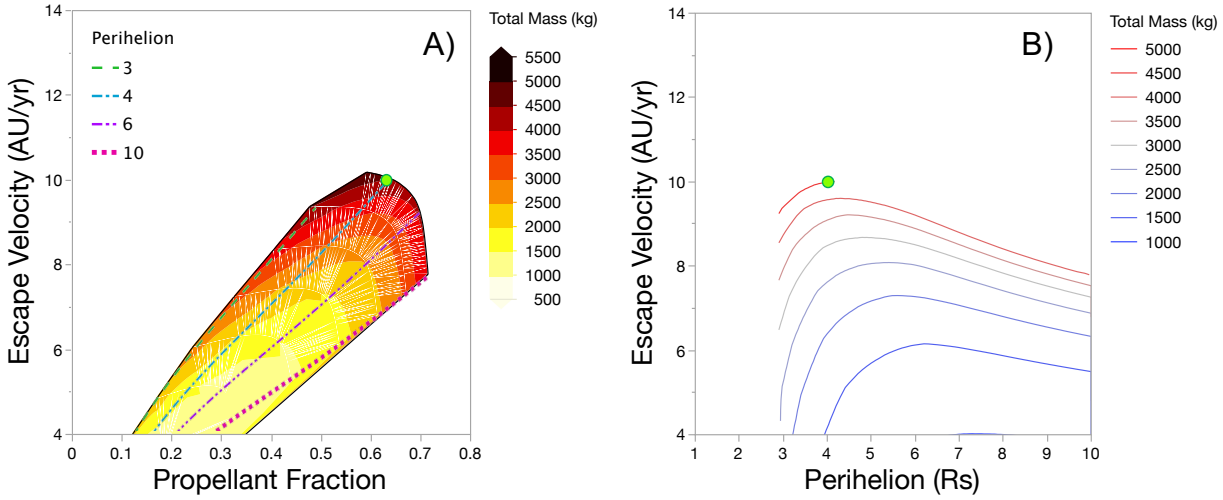

Figure 36. *A) The escape velocity is plotted versus propellant fraction for ammonia for different perihelions ranging from 3 to 10 R_s. The heat map behind the plots displays the total system mass that corresponds to the given escape velocity. B) The escape velocity is plotted versus perihelion for different total system masses, ranging from 1000 kg to 5000 kg. The maximum system mass is limited to 5000 kg, and the maximum surface temperature is limited to 2700 K. The green dot identifies the maximum escape velocity of 10.0 AU/yr at a perihelion of 4.2 R_s.*

3.1.9.1. Methane

The final propellant under consideration is methane. Methane was initially expected to be a strong contender due to the wide use of liquid natural gas (LNG) propulsion systems. Its specific impulse was also more competitive with hydrogen relative to the other propellants. However, the need for cryogenic storage made it less attractive once the full system was considered. As before, Figure 37A shows the escape velocity versus propellant fraction, and Figure 37B displays the escape velocity versus perihelion. It was actually the worst performing propellant, with a maximum escape velocity of 9.3 AU/yr at a perihelion of 4.1 R_s.

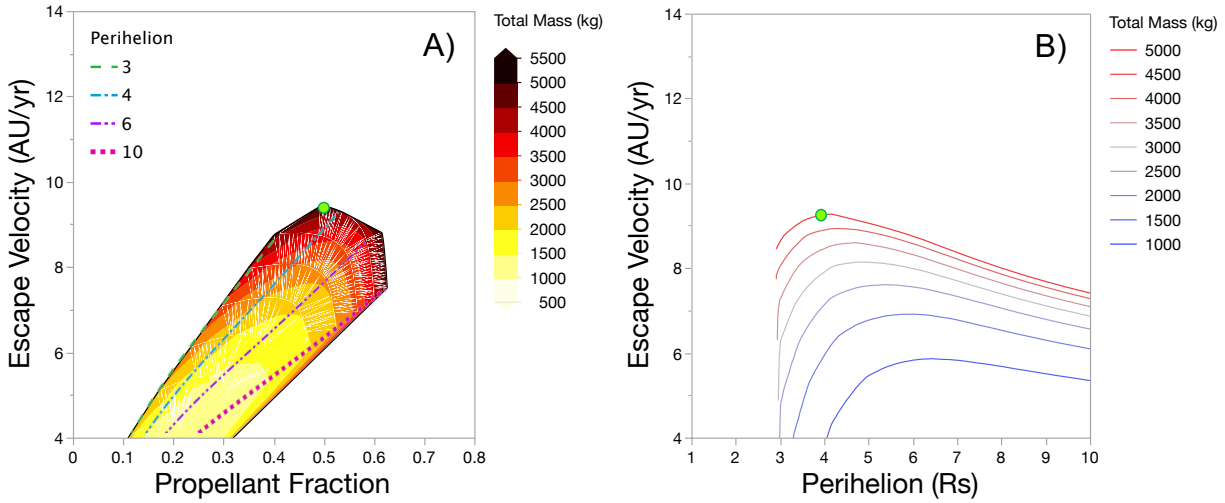

Figure 37. *A) The escape velocity is plotted versus propellant fraction for methane for different perihelions ranging from 3 to 10 R_s. The heat map behind the plots displays the total system mass that corresponds to the given escape velocity. B) The escape velocity is plotted versus perihelion for different total system masses, ranging from 1000 kg to 5000 kg. The maximum system mass is limited to 5000 kg, and the maximum surface temperature is limited to 2700 K. The green dot identifies the maximum escape velocity of 9.3 AU/yr at a perihelion of 4.1 R_s.*

4. Conclusion

The results of this study are summarized in Figure 38. Lithium hydride was the best performing propellant, with a maximum predicted escape velocity of 12.3 AU/yr at a perihelion of 4.5 R_s. Despite having a lower specific impulse than hydrogen, the much smaller mass penalty of its propellant storage and handling system more than made up for it. Lithium similarly had a higher escape velocity than hydrogen (10.7 AU/yr) due to its relatively lightweight storage system.

Also outperforming hydrogen was ammonia. It had a maximum escape velocity of 10.0 AU/yr at a perihelion of 4.0 R_s. Although it may be tempting to select lithium hydride in order to attain as great a velocity as possible, ammonia is attractive from the standpoint of TRL advancement. It allows for cheaper, safer test conditions, which will allow prototype development to continue at a faster pace. Perhaps more important is the fact that TRL advancement could focus solely on the survivability and function of the heat shield rather than splitting attention among the heat shield, storage tank, and flow control system. Furthermore, high temperature ammonia does not appear to undergo any obvious, unwanted side reactions that cannot be mitigated with refractory barrier coatings.

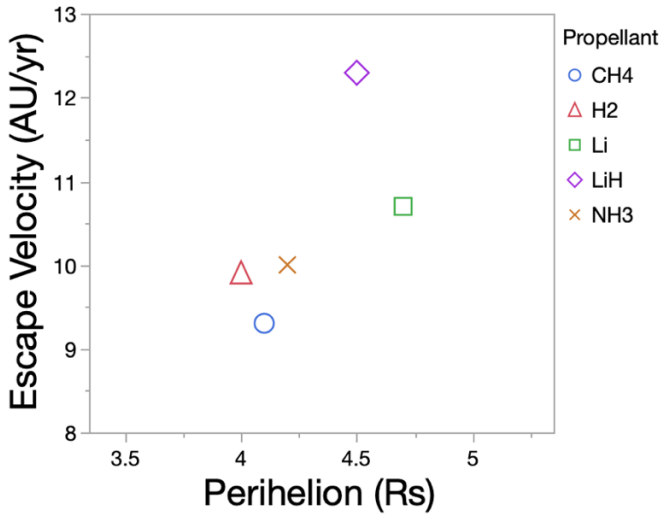

Figure 38. *The maximum escape velocity is plotted versus perihelion for each propellant with a total mass limit of 5000 kg and a maximum operating temperature limit of 2700 K.*

The original goal of this study was to determine whether it was feasible to achieve an escape velocity of 20 AU/yr from the solar system. Initial calculations were largely unconstrained by considerations of the maximum payload of an SLS rocket, and the design assumptions were chosen to be as lightweight as possible. In this study, we wanted to perform the calculations in a way that did not add any additional low TRL technologies to an already unconventional approach. We assumed that the operating temperature would be no higher than 2700 K, we assumed that the maximum payload of an SLS rocket would remain below 5000 kg, we chose a high value for the rocket chamber pressure, and we selected a relatively common aluminum alloy for the propellant tanks.

Our new goal, then, is to understand what the performance would look like if a combined heat shield and solar thermal propulsion system were pursued for the next 5-10 years. These escape velocities do not represent the greatest potential performance that this approach could produce, but rather the best performance that we could expect if we focused solely on the development of a heat shield that doubles as a heat exchanger for a solar thermal propulsion system. We note this here, because the highest escape velocity was only 1.7x greater than a passive gravity assist around Jupiter with an SLS rocket. Our previous calculations yielded something closer to a doubling of the escape velocity with a more optimistic set of assumptions.

In some ways, the current calculations are a greater cause for optimism than the original result. We had been predicting an escape velocity under a perhaps unrealistic assumption that we would pursue a family of technology advancements to provide a major leap in the maximum escape velocity from the solar system. Here we argue that we can exceed 10 AU/yr by focusing on relatively straightforward modifications of the Parker Solar Probe thermal protection system heritage design. One has to consider, then, that a simpler design using ammonia propellant would merely be the first step among future systems that will have a much higher ceiling than a passive gravity assist. The solar Oberth maneuver has been shown to offer much greater speeds with more aggressive optimization, and it offers some intriguing side benefits for heliophysics due to the much closer approach to the Sun afforded by its active cooling and shorter residence time.

5. References

1. Runyon, K., Holler, B., & Bannister, M. (2020, September). Exploring Trans-Neptunian Objects with Interstellar Probe. In *European Planetary Science Congress* (pp. EPSC2020-276).
2. W. Schlei, J. Atchison, R. Gomez-Cano, B. Lathrop and B. Villac, "Pragmatic Trajectory Options Applicable to an Interstellar Probe Mission," *2021 IEEE Aerospace Conference (50100)*, **2021**, pp. 1-15, doi: 10.1109/AERO50100.2021.9438398.
3. Oberth H, *Ways to Spaceflight*, Verlag, Berlin, **1929**; also *NASA technical translation* TT F-622, **1972**.
4. Shoji J, Frye P. Solar thermal propulsion for orbit transfer. in *24th Joint Propulsion Conference* **1988**, 3171.
5. Lyman R, Ewing M, Krishnan R, Lester D, McNutt, Jr R. Solar thermal propulsion for an interstellar probe. in *37th Joint Propulsion Conference and Exhibit* **2001**, 3377.
6. Santo AG, Gold RE, McNutt Jr RL, Solomon SC, Ercol CJ, Farquhar RW, Hartka TJ, Jenkins JE, McAdams JV, Mosher LE, Persons DF. The MESSENGER mission to Mercury: spacecraft and mission design. *Planetary and Space Science*. **2001**, *49*(14-15), 1481-500.
7. McNutt, RL, A Realistic Interstellar Explorer, NIAC 7600-039 Final Report, October 23, **2003**.
8. NRC, *The Sun to the Earth - and Beyond: A Decadal Research Strategy in Solar and Space Physics*. Washington, DC: The National Academies Press. **2003**, https://doi.org/10.17226/10477.
9. NRC, *Solar and Space Physics: A Science for a Technological Society*. Washington, DC: The National Academies Press. **2013**, https://doi.org/10.17226/13060.
10. Simpson, J.A., Chamberlain, J.W., Kraushaar, W., et al. **1960**, Interim Report No. 3. Washington, DC: Space Science Board.
11. Glaister D, Schmidt J, McLean C, Mills G. Long term cryogenic storage technologies overview for NASA exploration applications. In *42nd AIAA Thermophysics Conference.* **2011** (p. 3774).
12. Chase, M.W., Jr., NIST-JANAF *Themochemical Tables, Fourth Edition*, J. Phys. Chem. Ref. Data, Monograph 9, **1998**, 1-1951
13. Wilner, B., Hays, L., and Buhler, R., “Research and Development Studies to Determine Feasibility of a Solar LH2 Rocket Propulsion System (SOHR),” *Contract Report AF04611-8181*, Electro-Optical Systems, Pasadena CA, September **1963**.
14. Zhumaev ZS, Shcheglov GA. Operations dynamics analysis of solar thermal propulsion for CubeSats. *Advances in Space Research*. **2019** Aug 15; *64*(4): 815-23.
15. Nakamura T, Sullivan D, McClanahan J, Shoji J, Partch R, Quinn S. Solar thermal propulsion for small spacecraft. In *40th AIAA/ASME/SAE/ASEE Joint Propulsion Conference and Exhibit.* **2004** Jul (p. 4138).

16. Leverone F, Cervone A, Gill E. Cost analysis of solar thermal propulsion systems for microsatellite applications. *Acta Astronautica*. **2019** Feb 1; *155*: 90-110.

17. Ehricke KA. The solar-powered space ship. General Dynamics/Astronautics, San Diego, CA; AD0830567, **1959** Jan 1.

18. Shoji, J. M., "Performance Potential of Advanced Solar Thermal Propulsion," Paper AIAA-83-1307, *AIAA/SAE/ASME 19th Joint Propulsion Conference*, Seattle, WA, June **1983**.

19. Etheridge FG. Solar rocket system concept analysis. Rockwell International, Downey CA Satellite Systems Division Space Systems Group; *final technical report for Air Force Rocket Propulsion Laboratory*, AFRPL-TR-79-79 ADA079117, **1979** Dec 1.

20. Fan JC. Selective-black absorbers using sputtered cermet films. *Thin Solid Films*. **1978** Oct 16; *54*(2): 139-48.

21. Selvakumar N, Barshilia HC. Review of physical vapor deposited (PVD) spectrally selective coatings for mid-and high-temperature solar thermal applications. *Solar energy materials and solar cells.* **2012** Mar 1; *98*: 1-23.

22. Shoji JM. Potential of Advanced Solar Thermal Propulsion. *Orbit Raising and Maneuvering Propulsion: Research Status and Needs*. **1984**, *89*, 30-47.

23. Yu ST, Chang CL, Merkle C. Solar rocket plume/mirror interactions. In *22nd Joint Propulsion Conference* **1991** Jan 1, 1433.

24. Wong, W. A., Geng, S. M., Castle, C. H., and Macosko, R. P., "Design, Fabrication and Test of a High Efficiency Refractive Secondary Concentrator for Solar Application," Paper AIAA 2000-1998, *38th AIAA Aerospace Science Meeting and Exhibit*, Reno, NV, January **2000**.

25. Sauder J, Preudhomme M, Mueller J, Cheikh D, Sunada E, Karimi RR, Couto A, Arora N, Rapinchuk J, Alkalai L. System Engineering a Solar Thermal Propulsion Mission Concept for Rapid Interstellar Medium Access. *Advances in Astronautics Science and Technology*. **2021** Jun; *4*: 77-90.

26. Karimi R, Predudhomme M, Cheikh D. Mission design for a solar system fast escape to interstellar medium, solar-gravity lens focus, and beyond. In *AGU Fall Meeting Abstracts 2020* Dec; **2020**, pp. SH017-0009.

27. Landau D, Donitz B, Karimi R. Near-term strategies to rendezvous with an interstellar object. *Acta Astronautica*. **2023** Feb 16, https://doi.org/10.1016/j.actaastro.2023.02.021.

28. Garwin RL. Solar sailing-a practical method of propulsion within the solar system. *Jet Propulsion*. **1958** Jan 1; *28*(3): 188-90.

29. Bailer-Jones CA. The sun diver: Combining solar sails with the Oberth effect. *American Journal of* Physics. **2021** Mar; *89*(3): 235-43.

30. Macdonald M, McInnes C. Solar sail science mission applications and advancement. *Advances in Space Research*. **2011** Dec 1; *48*(11): 1702-16.

31. Youngquist RC, Nurge MA. Solar Surfing: Final Report on a Phase I NASA Innovative Advanced Concepts Study. **2018** Apr 1.

32. Davoyan AR, Munday JN, Tabiryan N, Swartzlander GA, Johnson L. Photonic materials for interstellar solar sailing. *Optica*. **2021** May 20; *8*(5): 722-34.
33. Srivastava PR, Swartzlander GA. Optomechanics of a stable diffractive axicon light sail. *The European Physical Journal Plus*. **2020** Jul; *135*(7): 1-6.
34. Spieth D, Zubrin R. Ultra-Thin Solar Sails for Interstellar Travel–Phase I Final Report. *NASA Institute for Advanced Concepts*, Pioneer Astronautics Inc. **1999** Dec.
35. Kumar S, Thomas L, Cassibry JT, Frederick RA. Review of nuclear thermal propulsion technology for deep space missions. In *AIAA Propulsion and Energy 2020 Forum* **2020**; 3915.
36. Hibberd A, Hein AM. Project lyra: catching 1I/'Oumuamua–using nuclear thermal rockets. *Acta Astronautica*. **2021** Feb 1; *179*: 594-603.
37. Noble RJ. Radioisotope electric propulsion of sciencecraft to the outer solar system and near-interstellar space. *Acta Astronautica*. **1999** Jan 1; 44(2-4): 193-9.
38. McNutt, RL, et al., Interstellar probe study 2019 report, **2019**, NASA Task order NNN06AA01C.
39. McNutt, R.L., Jr., Benson, W.W., Gruntman, M., Krimigis, S.M., Roelof, E.C., Vernon, S.R., Wimmer-Schweingruber, R.F. Enabling Interstellar Probe: Space Launch System (SLS) trades. Paper presented at the 66th International Astronautical Congress, Jerusalem, Israel. **2015**.
40. Cantelo RC. The thermal decomposition of methane. *The Journal of Physical Chemistry*. **2002** May 1; 28(10): 1036-48.
41. Chen SQ, Wang HX. Transport properties of lithium plasma. *Chinese Physics Letters*. **2012** Feb 1; 29(2): 025202.
42. Walter PL, Rushinko FR, Austin, LG. Gas reaction of carbon. *Advances in Catalysis*. **1959** 11, 133-221.
43. Morrell JC, inventor. Lithium rocket propellants and process for using the same. United States patent US 3,153,902. **1964** Oct 27.
44. Gibb TRP, Messer CE. A survey report on lithium hydride. Department of Chemistry, Tufts College; **1954**, vol. 3957.
45. Messer CE. A survey report on lithium hydride. United States Atomic Energy Commission, Technical Information Service; **1960**.
46. Pasman H in *Risk Analysis and Control for Industrial Processes - Gas, Oil and Chemicals A System Perspective for Assessing and Avoiding Low-Probability, High-Consequence Events.* Edited by Pasman H, Butterworth-Heinemann*,* **2015**, 1-31
47. Howell JR, Mengüç MP, Daun K, Siegel R. *Thermal radiation heat transfer*. CRC press; **2020** Dec.
48. R. R. Hibbard, "Equilibrium temperatures of ideal spectrally selective surfaces," *Solar Energy*, vol. 5, pp. 129-132, 1961.

49. M. J. Riedl, *Optical design fundamentals for infrared systems,* SPIE press, **2001**. https://doi.org/10.1117/3.412729.

50. J. Stefan, "Über di Beziehung zwischen der Wärmestrahlung und der Temperatur [On the relationship between heat radiation and temperature]," *Sitzungsberichte der Mathematisch-naturwissenschaftlichen Classe der Kaiserlichen Akademie der Wissenschaften*, vol. 79, pp. 391-428, **1879**.

51. L. Boltzmann, "Ableitung des Stefanschen Gesetzes, betreffend die Abhängigkeit der Wärmestrahlung von der Temperatur aus der Electromagetischen Lichttheorie [Derivation of Stefan's little law concerning the dependence of thermal radiation on the temperature of the elect," *Annalen der Physik und Chemie*, vol. 258, pp. 291-294, **1884**.

52. M. Planck, *The theory of heat radiation* (translation), P. Masius, Ed., Philadelphia: Backiston's Son & Company, **1914**.

53. R. L. McNutt Jr, R. F. Wimmer-Schweingruber, M. Gruntman, S. M. Krimigis, E. C. Roelof, P. C. Brandt, S. R. Vernon, M. V. Paul, B. W. Lathrop, D. S. Mehoke and D. H. Napolillo, "Near-term interstellar probe: First step," *Acta Astronautica*, vol. 162, pp. 284-299, **2019**.